Mutually suppressive roles of KMT2A and KDM5C in behaviour, neuronal structure, and histone H3K4 methylation

Christina N. Vallianatos[1, 2], Brynne Raines[3], Robert S. Porter[1,2], Katherine M. Bonefas[1,4], Michael C. Wu[5], Patricia M. Garay[1,4], Katie M. Collette[3], Young Ah Seo[6], Yali Dou[7], Catherine E. Keegan[1,8], Natalie C. Tronson[3,*], and Shigeki Iwase[1,*]

[1]Department of Human Genetics, Michigan Medicine, University of Michigan, Ann Arbor, MI 48109

[2]Genetics and Genomics Graduate Program, University of Michigan, Ann Arbor, MI 48109

[3]Department of Psychology, College of LS&A, University of Michigan, Ann Arbor, MI 48109

[4]The University of Michigan Neuroscience Graduate Program

[5]Neurodigitech, LLC, San Diego, CA

[6]Department of Nutritional Sciences, School of Public Health, University of Michigan, Ann Arbor, MI 48109

[7]Department of Pathology, Michigan Medicine, University of Michigan, Ann Arbor, MI 48109

[8]Department of Pediatrics, Michigan Medicine, University of Michigan, Ann Arbor, MI 48109

*Co-corresponding authors

Please address correspondence to: siwase@umich.edu and ntronson@umich.edu

Abstract

Histone H3 lysine 4 methylation (H3K4me) is extensively regulated by numerous writer and eraser enzymes in mammals. Nine H3K4me enzymes are associated with neurodevelopmental disorders to date, indicating their important roles in the brain. However, interplay among H3K4me enzymes during brain development remains largely unknown. Here, we show functional interactions of a writer-eraser duo, *KMT2A* and *KDM5C*, which are responsible for Wiedemann-Steiner Syndrome (WDSTS), and mental retardation X-linked syndromic Claes-Jensen type (MRXSCJ), respectively. Despite opposite enzymatic activities, the two mouse models deficient for either *Kmt2a* or *Kdm5c* shared reduced dendritic spines and increased aggression. Double mutation of *Kmt2a* and *Kdm5c* clearly reversed dendritic morphology, key behavioral traits including aggression, and partially corrected altered transcriptomes and H3K4me landscapes. Thus, our study uncovers common yet mutually suppressive aspects of the WDSTS and MRXSCJ models and provides a proof of principle for balancing a single writer-eraser pair to ameliorate their associated disorders.

Introduction

Dysregulation of histone methylation has emerged as a major contributor to neurodevelopmental disorders (NDDs) such as autism spectrum disorders and intellectual disabilities (1). Histone methylation can be placed on a subset of lysines and arginines by histone methyltransferases (writer enzymes) and serves as a signaling platform for a variety of nuclear events including transcription (2). Reader proteins specifically recognize methylated histones, thereby converting methylation signals into higher-order chromatin structures. Histone methylation can be removed by a set of histone demethylases (eraser enzymes). Pathogenic variants in all three classes of methyl-histone regulators cause NDDs, indicating critical, yet poorly understood roles of histone methylation dynamics in brain development and function (3).

Histone H3 lysine 4 methylation (H3K4me) is one of the most well-characterized histone modifications. H3K4me is primarily found at transcriptionally active areas of the genome. The three states, mono-, di-, and tri-methylation (H3K4me1-3), uniquely mark gene regulatory elements and play pivotal roles in distinct steps of transcription. While H3K4me3/2 are enriched at transcriptionally engaged promoters, H3K4me1 is a hallmark of transcriptional enhancers (4, 5). At promoters, H3K4me3 contributes to recruitment of general transcription machinery TFIID and RNA polymerase II (6, 7). H3K4me1 at enhancers can be recognized by BAF, an ATP-dependent chromatin remodeling complex (8).

H3K4me is extensively regulated by more than seven methyltransferases and six demethylases in mammals (9). Consistent with the important roles of H3K4me in transcriptional regulation, genomic distribution of H3K4me appears highly dynamic during brain development (10). However, the contributions of each of the 13 enzymes in the dynamic H3K4me landscapes of the developing brain remain largely unknown. Strikingly, genetic alterations in nine H3K4me enzymes and at least two H3K4me readers have been associated with human NDDs to date, indicating the critical roles of H3K4me balance (10) (Figure 1A). These human conditions can be collectively referred to as brain H3K4 methylopathies and point to non-redundant yet poorly understood roles of these genes controlling this single post-translational modification for faithful brain development. Of note, some of these enzymes can have non-enzymatic scaffolding function (11) as well as non-histone substrate (12); therefore, these disorders may potentially involve mechanism outside histone H3K4 methylation.

As histone modifications are reversible, one can, in theory, correct an imbalance by modulating the writers or erasers. Chemical inhibitors of histone deacetylases (HDACs) have been successfully used to rescue phenotypes in mouse models of NDDs. HDAC inhibitors were able to ameliorate learning disabilities in mouse models of Rubinstein-Taybi and Kabuki syndromes, which are deficient for CREBBP or KMT2D, writer enzymes for histone acetylation or H3K4me, respectively (13, 14). However, the HDAC inhibitors, such as SAHA and AR-42, used in these studies interfere with multiple HDACs (15), which could potentially result in widespread side effects. Given the non-redundant roles of the H3K4me enzymes, a more specific perturbation is desirable.

In order to achieve specific modulation of H3K4me, an important first step is to delineate functional relationships between the H3K4 enzymes. Focus of the work is on a pair of NDD-associated writer/eraser enzymes: KMT2A and KDM5C. Haploinsufficiency of *KMT2A* underlies Weidemann-Steiner Syndrome (WDSTS), characterized by developmental delay, intellectual disability, characteristic facial features, short stature, and hypotonia (16). Loss of KDM5C function defines Mental Retardation, X-linked, syndromic, Claes Jensen type (MRXSCJ), in which individuals display an intellectual disability syndrome with aggression, short stature, and occasional autism comorbidity (17). Mouse models have provided experimental support for causative impacts of KMT2A and KDM5C deficiencies in impaired cognitive development (18-22). Social behavior and neuronal structure in *Kmt2a*-KO mice however have not been characterized.

In the present work, we tested whether modulating a single H3K4me writer or eraser can ameliorate the neurodevelopmental symptoms observed in the WDSTS and MRXSCJ mouse models. We generated *Kmt2a*-, *Kdm5c*-double mutant (DM) mice, and performed systematic comparisons between wild-type (WT), single mutants, and DM mice.

Results

KMT2A and KDM5C co-exist broadly in the brain

We first examined expression patterns of KMT2A and KDM5C using publicly available resources, and found the two genes are broadly expressed throughout brain regions of adult mice and humans (Supplementary Figure 1). *Kmt2a* and *Kdm5c* are expressed at comparable levels in all major excitatory and inhibitory neuron subtypes as well as glia cells in mouse visual cortices (Supplementary Figure 1A), and also throughout mouse brains (Supplementary Figure 1B). Consistently, developing and aging human brains express *KMT2A* and *KDM5C* at high, steady levels (Supplementary Figure 1C). Thus, both writer and eraser are co-expressed across brain cell types, regions, and developmental stages in both humans and mice.

Generation of *Kmt2a-Kdm5c* double-mutant (DM) mice

To test genetic interaction of *Kmt2a* and *Kdm5c*, we generated *Kmt2a-Kdm5c* double-mutant (DM) mice. Experimental mice were F1 hybrids of the two fully congenic strains: 129S1/SvImJ *Kmt2a*$^{+/-}$ males (23) and C57BL/6J *Kdm5c*$^{+/-}$ females (21) (Figure 1B). This cross resulted in the following genotypes of male mice in an identical genetic background: wildtype (WT); *Kmt2a* heterozygote (*Kmt2a*-HET: *Kmt2a*$^{+/-}$), *Kdm5c* hemizygous knock-out (*Kdm5c*-KO: *Kdm5c*$^{-/y}$), and *Kmt2a-Kdm5c* double-mutant (DM: *Kmt2a*$^{+/-}$, *Kdm5c*$^{-/y}$), thereby allowing us to perform a comparison between the WDSTS model (*Kmt2a*-HET), the MRXSCJ model (*Kdm5c*-KO), and their composite (DM). We

125 focus on males, because MRXSCJ predominantly affects males and *Kdm5c*-
126 heterozygous female mice exhibit only minor cognitive deficits (22).
127
128 These mice were born at expected Mendelian ratios of 25% per genotype,
129 demonstrating the DM mice were not synthetic lethal (Figure 1C). Genotypes were
130 confirmed at RNA and DNA levels (Supplementary Figure 1A-C), and protein level for
131 KDM5C (Supplementary Figure 1D). Brain anatomy showed no gross deformities in any
132 of the genotypes (Supplementary Figure 1E). Both *Kmt2a*-Het and *Kdm5c*-KO mice
133 showed significant body weight reduction compared to WT (Figure 1D and
134 Supplementary Figure 1F, One Way ANOVA: $F(3, 55) = 10.28$, $p < 1.0 \times 10^{-4}$, Tukey's
135 multiple comparison test: WT vs 2A: $p = 0.008$, WT vs 5C: $p = 0.008$). DM body weight
136 was significantly smaller compared to WT (DM vs WT: $p < 1.0 \times 10^{-4}$). Thus, loss of
137 *Kdm5c* and *Kmt2a* heterozygosity both led to growth retardation, which was not
138 corrected but rather slightly exacerbated in DM mice. Note that for all the four-way
139 comparisons in this study, we first represent the *p*-values from one-way ANOVA tests of
140 genotype-phenotype interaction with histograms. We then report *p*-values from post-hoc
141 tests of all six genotype comparisons with 95% confidence intervals of group mean
142 differences.
143
144 **Memory impairments in *Kdm5c*-KO were ameliorated in DM**
145 We first sought to determine the effect of loss of *Kmt2a* and/or *Kdm5c* on mouse
146 behavior through a battery of behavioral tests. Learning and memory was measured by
147 two independent tests, contextual fear conditioning (CFC) and novel object recognition

(NOR). In CFC, we observed a significant effect of genotype (CFC: F (3,60) = 4.133, p = 0.010). In accordance with previous findings (21, 22), *Kdm5c*-KO showed significant deficits in associative fear memory in CFC (Figure 2A, WT vs 5C: p = 0.017, 2A vs 5C: p = 0.0.024). Previous work reported that homozygous deletion of *Kmt2a* in excitatory hippocampal neurons leads to impaired fear memory in the CFC (20). In contrast, *Kmt2a*-HET mice showed no deficits in either CFC or NOR (Figure 2A-B) (CFC: p = 1.000), indicating that *Kmt2a*-heterozygosity does not lead to learning impairment measured in these assays. Importantly, DM mice did not differ from WT mice (Figure 2A) (p = 0.923), suggesting that *Kmt2a* heterozygosity rescues CFC memory deficits of *Kdm5c*-KO mice.

A similar pattern emerged in NOR, where we observed a significant main effect of genotype (F(3,64) = 3.20, p = 0.030). Here, *Kdm5c*-KO mice showed significantly less preference for the novel object than other genotypes (Figure 2B) (WT *vs* 5C: p = 0.041; 2a *vs* 5C: p = 0.091). Consistent with our CFC results, neither *Kmt2a*-HET mice nor DM mice differed from WT mice (p = 1.000), suggesting that *Kmt2a* heterozygosity does not impair memory, but can rescue impairments of *Kdm5c*-KO. Importantly, WT, *Kmt2a*-Het, and DM mice showed preference for the novel object (Z = 2.029; p = 0.041). Nevertheless, as this was not a strong preference, it is likely that non-mnemonic effects, including anxiety processes, also contributed to avoidance-like behavior in *Kdm5c*-KO mice. Differences between genotypes in memory tasks were not attributable to locomotor activity or shock responsiveness, as none of these parameters showed significant differences among the genotypes (Figure 2C-D).

171

172 **Social behavior in the single and double mutants**

173 We next examined social behavior using the three independent behavioral paradigms.
174 First, social interaction was tested with the three-chambered preference test, with an
175 overall effect of genotype ($F(3,60) = 3.726$, $p = 0.016$). WT mice showed a robust
176 preference for the novel mouse over the toy mouse ($Z = 2.97$, $p = 0.003$). Consistent
177 with previous studies (21), *Kdm5c*-KO mice exhibited significantly less preference for
178 the stranger mouse compared with WT (WT vs 5C: $p= 0.023$); whereas *Kmt2a*-HET
179 mice showed no differences from WT (Figure 3A, WT vs 2A: $p = 0.563$) (20). Similar to
180 *Kdm5c*-KO, DM mice showed a strong trend towards less time with stranger mice
181 compared to WT (WT vs DM: $p = 0.077$). No difference was detected between *Kdm5c*-
182 KO and DM (5C vs DM: $p= 1.000$), indicating that *Kmt2a* heterozygosity does not alter
183 social preference or rescue the deficit of *Kdm5c*-KO.

184

185 In tests of social dominance (Figure 3B), both *Kmt2a*-HET and *Kdm5c*-KO mice won
186 more frequently against WTs (2A vs WT: 60.9%, $p = 0.091$, 5C vs WT: 68.4%, $p =$
187 0.008). In contrast, DM animals lost more than 80% of their bouts against WT (DM vs
188 WT: $p = 1.47 \times 10^{-5}$). Although DM mice were slightly smaller compared to single
189 mutants (Figure 1D), this is unlikely to drive submissive behaviors, as body mass has
190 been shown to have minimal impact on social hierarchy unless excess difference (>
191 30%) is present between animals (24), which is not the case in our study (Figure 1D)
192 (2A vs WT:11%, 5C vs WT: 17%, DM vs WT: 25%). These results indicate that the two

single mutants share heightened social dominance and the double mutation reverses the social dominance.

Lastly, in the resident-intruder test, similar to other behavioral paradigms, overall effects of genotype were evident in both aggressive and submissive behavior (Figure 3C, aggressive behavior: $F(3,60) = 3.642$, $p = 0.018$; aggression x genotype: $F(12,240) = 1.853$, $p = 0.041$; submissive behavior: ($F(3,60) = 4.335$, $p = 0.008$). The genotype effect on aggressive behaviors inversely correlated with that of submissive behavior, reinforcing the changes in specific behaviors rather than general locomotor activity. Both *Kmt2a*-HET and *Kdm5c*-KO showed a trend of increased aggression and decreased submission when we combined frequency of all aggressive or submissive behavior types compared to WT (Figure 3C).

DM mice showed significantly reduced overall aggression compared to the two single mutants (Fig. 3C, DM vs 5C: $p = 0.045$, DM vs 2A: $p = 0.051$). Reciprocally, DM mice were more submissive compared to single mutants (DM vs 5C: $p = 0.006$, DM vs 2A: $p = 0.059$). Comparison between DM and WT mice did not yield any significant differences. The decreased aggression and increased submission of DM relative to the single mutants were also observed in multiple behavior types, including mounting, chasing for aggression (Supplementary Figure 3A), and cowering and running away for submission (Supplementary Figure 3B). Thus, these results suggest that double mutations alleviate aggressive behavior of both *Kmt2a*-HET and *Kdm5c*-KO mice.

Together, the behavioral studies revealed more pronounced deficits in *Kdm5c*-KO animals compared to *Kmt2a*-HET mice in terms of memory and social interaction, while *Kmt2a*-HET and *Kdm5c*-KO mice shared increased social dominance and aggression. The consequences of double mutations varied between the tests, with clear rescue effects on cognitive tasks, dominant behavior, and aggression, and no effect on social interactions. No behavioral traits were exacerbated in DM. Interestingly, DM mice showed opposite phenotypes in social dominance and aggression compared to single mutants, which is reminiscent of the increased spine density in the DM basolateral amygdala but not in the hippocampal CA1 (Figure 4). These results establish common and unique behavioral deficits of *Kdm5c*-KO and *Kmt2a*-HET mice and mutual suppression between the two genes in some of the traits.

Roles of KMT2A, KDM5C, and their interplay in neuronal morphology

Altered dendrite morphology is a hallmark of many human NDDs, as well as animal models of NDDs (25). We previously found reduced dendritic length and spine density in basolateral amygdala (BLA) neurons of *Kdm5c*-KO adult male mice (21). Assessment of dendritic morphology in *Kmt2a*-HET has not been reported. We first performed comparative dendrite morphometry of pyramidal neurons in the BLA using Golgi staining for the four genotypes (Figure 4). For *Kdm5c*-KO neurons, we recapitulated our previous findings of reduced dendrite lengths (Figure 4A and B, one-way ANOVA followed by Tukey's multiple comparison test, WT vs 5C: $p = 0.034$) and lower spine density (Figure 4A and C, WT vs 5C: $p = 0.008$). Similar to *Kdm5c*-KO neurons, *Kmt2a*-

HET cells exhibited a reduction in spine density (Figure 4B and C, WT vs 2A: p = 0.005) but not in dendritic length (WT vs 2A: p = 0.177).

Dendrite lengths of DM did not differ significantly from WT (Figure 4B, WT vs. DM: p = 0.550); however, these lengths were also not different from *Kdm5c*-KO (*Kdm5c*-KO vs. DM: p = 0.534), representing a weak restorative effect. In contrast, dendritic spine density of DM showed a significant increase that surpassed a rescue effect (Figure 4C). As morphology of dendritic spines progressively changes during synaptogenesis and development, we also asked whether developmental subtypes of dendritic spines were altered in any genotype. We did not find dramatic changes in spine morphology among the four genotypes (Figure 4D, Supplementary Figure 4), indicating selective requirement of *Kdm5c* and *Kmt2a* for regulation of spine numbers.

Since the ventral hippocampus CA1 (vCA1) receives inputs from BLA (26), we also performed morphometry analyses of pyramidal neurons in this region. Genotype had significant impact on dendritic spine density (one-way ANOVA, F (3, 92) 11.51, $p < 1.0 \times 10^{-4}$) but not on dendritic length (F (3, 92) = 0.564, p=0.639). While dendritic length did not show any difference in *Kdm5c*-KO and *Kmt2a*-HET neurons, spine density was decreased in the two single mutants compared to WT (WT vs 2A: $p = 2.0 \times 10^{-4}$, WT vs 5C: $p < 1.0 \times 10^{-4}$).

In DM vCA1, spine density showed a trend of degrease compared to WT, yet this did not reach statistical significance (WT vs DM: p = 0.066). DM spine density was

261 significantly higher than *Kdm5c*-KO (DM vs 5C: p = 0.021) but similar to *Kmt2a*-HET
262 (DM vs 2A: p=0.223). These analyses indicate reduced spine density in both *Kdm5c*-KO
263 and *Kmt2a*-HET vCA1 neurons and its partial correction in DM.
264
265 Overall, we conclude that *Kmt2a*-HET and *Kdm5c*-KO share a reduced spine density in
266 both BLA and vCA1. Double mutations led to reversal of spine phenotype in BLA and
267 partial restoration in vCA1, supporting mutually suppressive roles of KMT2A and
268 KDM5C in dendritic spine development.
269
270 **Roles of KMT2A and KDM5C in mRNA expression**
271 *Kdm5c*-KO mice exhibit aberrant gene expression patterns in the amygdala and frontal
272 cortex (21), and hippocampus (22). Excitatory-neuron specific conditional *Kmt2a*-KO
273 mice were also characterized with altered transcriptomes in the hippocampus and
274 cortex (19, 20). However, the global gene expression of *Kmt2a*-HET, which is akin to
275 the WDSTS syndrome genotypes, has not been determined. To compare the impact of
276 *Kmt2a*-heterozygosity and *Kdm5c*-KO on the transcriptomes, we performed mRNA-seq
277 using the amygdala and the hippocampus of adult mice with four animals per genotype.
278 We confirmed the lack or reduction of reads from *Kdm5c* exons 11 and 12 and *Kmt2a*
279 exons 8 and 9 (Supplementary Figure 2A-B). The accurate microdissection of brain
280 regions was confirmed by co-clustering of our data with another published mRNA-seq
281 (27) (Supplementary Figure 5A). Principal component analysis (PCA) indicated that
282 transcriptomic divergence was primarily driven by brain regions rather than genotypes
283 (Supplementary Figure 6A)

284

285 In the amygdala, we identified 132 differentially expressed genes (DEGs) in *Kdm5c*-KO
286 (5C-DEGs) and no 2A-DEG (*padj* < 0.1, n =4, Figure 5A and Supplementary Figure 6).
287 The hippocampus yielded a consistently higher number of DEGs across the mutant
288 genotypes (344 5C-DEGs and 4 2A-DEGs). The small number of 2A-DEGs is likely due
289 to the one remaining copy of *Kmt2a*. Given increased social dominance (Figure 3B) and
290 clear reduction of dendritic spines (Figure 4) in *Kmt2a*-HET mice, we reasoned that
291 such phenotypes might be associated with mild gene misregulation, which was not
292 detected by DEseq2. To be able to analyze the gene expression in *Kmt2a*-HET, we set
293 a relaxed cut off ($p < 0.005$) and retrieved 78 and 139 genes as 2A-DEG from the
294 amygdala and hippocampus, respectively (Figure 5B and Supplementary Figure 6). We
295 found an overall similarity in gene misregulation between the two brain regions for both
296 *Kdm5c*-KO and *Kmt2a*-HET (Supplementary Figure 7A-B). Table S1 lists all DEGs
297 found in the study.

298

299

300 We next compared the gene expression profiles between the single mutants. The
301 majority of 5C-DEGs were upregulated and 2A-DEGs were downregulated (Figure 5A
302 and 5B, Supplementary Figure 6). This result agrees with KMT2A's primary role as a
303 transcriptional coactivator and KDM5C's suppressive activity on transcription by
304 removing this mark, yet KDM5C can also act as a positive regulator of transcription (28).
305 If KMT2A and KDM5C counteract, DEGs would be oppositely misregulated between the
306 single mutants. Indeed, we found that 28-29% of 5C-DEGs and 8-17% of 2A-DEGs

show signs of opposite regulation in the other single mutant (Supplementary Figure 8A-B). Substantial fractions of DEGs were misregulated in the same directions (Supplementary Figure 8A-B), which might be due to indirect consequences of gene manipulations and altered circuits.

Impact of double mutations on mRNA expression

If the double mutations fully restore the normal transcriptome, the DM transcriptome should resemble to that of WT over single mutants. However, the DM brain tissues had a similar number of DEGs as *Kdm5c*-KO (Figure 5A). Many DM-DEGs overlap with 5C-DEGs (84 in the amygdala and in the hippocampus), and 41 DM-DEGs overlap with 2A-DEGs in the hippocampus (Supplementary Figure 8C). Thus, the DM transcriptome still retains some mRNA misregulations of single mutants and does not fully return to the normal state.

To assess the rescue effect more quantitatively, we compared fold changes of single-mutant DEGs as a group between genotypes. Expression of 5C-up-regulated genes was significantly lower in the DM amygdala and hippocampus (Paired Wilcoxon signed-rank test, $p < 1.41 \times 10^{-8}$, Figure 5C). Reciprocally, expression of 2A-down-regulated genes was significantly higher in DM brain tissues ($p < 1.26 \times 10^{-8}$, Figure 5C). We further examined how individual DEGs behaved in DM. The fold changes of 5C-DEGs and 2A-DEGs in single mutants clearly correlated with those in DM, indicating that single-mutant DEGs are similarly dysregulated in DM in general. However, the slopes of linear regression were lower than 1 with statistical significance, suggesting the partial

rescue effect (Figure 5D). The mildest rescue effect was observed in 5C-DEGs in the DM amygdala (linear regression slope=0.91±0.03), while 5C-DEGs in the hippocampus and 2A-DEGs-R exhibit more pronounced rescue effects (slope: 0.51~0.73). These results indicate that misregulation of genes in both *Kdm5c*-KO or *Kmt2a*-HET was partially corrected in the DM brain tissues.

We then sought to isolate genes that might have contributed to the rescue effects at cellular and behavioral levels. As shown by the red circles in Figure 5D, some DEGs exhibit stronger rescue effects than others. We selected these genes as potential drivers of rescue effects (see Materials & Methods). While 10 genes in the amygdala and 81 genes in the hippocampus drove rescue effects of 5C-DEGs, 36 genes in the amygdala and 46 genes in the hippocampus contributed to the partial restoration of normal 2A-DEGs expression in DM (Supplementary Data 2). We then performed pathway analysis on these rescue-driving genes using the Enrichr program. While 2A-rescue genes did not yield any statistically significant enrichment (*padj* < 0.05), 5C-rescued genes showed an enrichment of a mouse KEGG pathway, “neuroactive ligand-receptor interaction” (*padj* = 5.60 x 10^{-3}, Odds ratio: 6.01). The following 10 genes contributed to the enrichment: *Pomc*, *Adcy2*, *Agt*, *Adora2a*, *Mc3r*, *Gabre*, *P2ry14*, *Tacr1*, *Trh*, *and Lhb*. Except for *P2ry14*, all these genes have known roles in learning and memory or aggression (Table 1). Many of these genes were expressed at low levels in the WT and were derepressed following the KDM5C loss (Supplementary Data 2), suggesting roles for KDM5C in suppressing aberrant gene expression.

353 Interestingly, most of these genes encode peptide hormones, their receptors, or
354 downstream signaling molecules. For example, Pro-opiomelanocortin (POMC) is a
355 peptide hormone primarily known for its roles in regulating hypothalamic functions, such
356 as feeding (29). In addition to its high expression in the hypothalamus, *Pomc* is also
357 expressed in the amygdala and the hippocampus (30). POMC signaling in these regions
358 has been implicated in the cognitive decline of Alzheimer's disease (31). Another gene
359 in the list, *Mc3r*, encodes a POMC receptor. *Mc3r* is expressed in the hypothalamus and
360 limbic structures such as the amygdala and hippocampus (32). Similar to *Pomc*, *Mc3r*'s
361 roles have been primarily studied in the hypothalamus, yet this gene has also been
362 implicated in hippocampal memory consolidation (33). Collectively, these results raise
363 the possibility that aberrant peptide hormone signaling and its normalization underlie
364 phenotypic outcomes of *Kdm5c*-KO and DM mice.
365
366 **H3K4me3 landscapes in WDSTS and MRXSCJ models**
367 We sought to determine the impact of KMT2A- and KDM5C-deficiencies and double
368 mutation on the H3K4me3 landscape within the amygdala. In Western blot analyses,
369 global H3K4me1-3 levels were not altered dramatically in any mutant (Figure 6A,
370 Supplementary Figure 9). We thus performed H3K4me3 chromatin immunoprecipitation
371 coupled with deep sequencing (ChIP-seq) to probe local changes genome-wide. To
372 assess the IP specificity, we spiked-in an array of recombinant nucleosomes carrying 15
373 common methylations along with DNA barcodes appended to the Widom601
374 nucleosome positioning sequence (34) (see Methods). The two recombinant H3K4me3
375 nucleosomes dominated the Widom601-containing DNA in all IP reactions with

376 negligible signals from other methylation states such as H3K4me1 or H3K4me2
377 (Supplementary Figure 10A), demonstrating a superb specificity of the ChIP.
378
379 PCA analyses of H3K4me3 distribution indicated that WT and *Kmt2a*-HET are close
380 each other, while *Kdm5c*-KO and DM cluster separately from the WT-2a-HET cluster.
381 Reminiscent of the transcriptome data (Figure 5), we did not recover any differentially
382 methylated regions (DMRs) in *Kmt2a*-HET, while *Kdm5c*-KO had 1,147
383 hypermethylated regions (Figure 6C, Supplementary Figure 9, padj < 0.05, see
384 method). In *Kdm5c*-KO, 583 loci are hypomethylated compared to WT, and these
385 regions are highly methylated regions in WT (Figure 6C and Supplementary Figure 10).
386 By relaxing the threshold, we obtained weak 2A-HET DMRs (Figure 6C, 357
387 hypermethylated and 240 hypomethylated). We then examined how these single-mutant
388 DMRs behaved in the other single mutant. Compared to the transcriptome data
389 (Supplementary Figure 8), we were able to recover more DMRs that are misregulated in
390 opposite directions between the single mutants (Figure 6D). These results suggest that,
391 as a primary substrate of the two enzymes, H3K4me3 changes represent the action of
392 KMT2A and KDM5C more directly compared to mRNA expression. Comparable
393 numbers of DMRs still show same-direction H3K4me3 changes, which may again
394 reflect indirect consequences of gene manipulations.
395
396 **Rescue effect of H3K4me3 landscapes in DM**
397 We next examined the impact of double mutations on H3K4me3 distributions. Notably,
398 in the PCA plot, the second replicate of DM showed a stronger rescued compare to

other replicates, indicating that expressivity of rescue effect varies among individual animals (Figure 6B). The number of DMRs in DM are smaller than those of single mutants, indicating a global rescue of aberrant H3K4me3 (Figure 6C). We then assessed how single-mutant DMRs behaved in DM. Note that, we focus on hypomethylated loci in *Kmt2a*-HET and hypermethylated loci in *Kdm5c*-KO (colored loci in Figure 6D) based on their enzymatic activities. The opposite-direction 2A-DMRs showed complete normalization in DM, while the same-direction 2A-DMRs were even more hypomethylated in DM (Figure 6E). Likewise, the opposite-direction 5C-DMRs showed more pronounced rescue effect in DM compared to same-direction 5C-DMRs (Figure 6E). This direction-dependent rescue effect persisted even when we omitted DM rep2 from the analysis (Supplementary Figure 11). These results strongly support the idea that KMT2A and KDM5C counteract to normalize H3K4me3 levels in specific genomic loci.

Peak annotation revealed that rescued DMRs tend to be outside the promoters, such as distal intergenic regions, introns, and internal exons (Figure 6F). ChIP-seq tracks of exemplary loci are represented in Supplementary Figure 12. Finally, we tested whether the rescue effects in gene expression involve normalization of H3K4me3. We took all rescued 2A-DEGs and plotted DM vs 2A fold changes of H3K4me3 as a function of DM vs 2A mRNA changes (Figure 6G). Rescued 2A-DEGs mostly showed an increase in mRNA levels in DM (Q2 and Q4). When mRNA expression increases from 2A-HET to DM, H3K4me3 levels also increase, which results in the larger number of genes within the upper right quadrant of the plot (Q2, 47 genes, $p < 1.0 \times 10^{-4}$, χ^2 test). Similarly,

422 when mRNA expression decreases from 5C-KO to DM, the majority of genes are
423 accompanied by decreased H3K4me3 nearby (Q3: 45 genes vs Q1: 20 genes, $p < 1.0 \times$
424 10^{-4}, χ^2 test). Furthermore, the magnitude of mRNA and H3K4me3 changes show
425 positive correlations (Pearson $r = 0.16$, and $r = 0.27$ for 2A- and 5C-DEGs,
426 respectively). Thus, misregulation of mRNA expression and its partial correction involve
427 corresponding restoration of the H3K4me3 levels.
428
429 **Discussion**
430 The present work, to our knowledge, represents the first genetic interactions between
431 mammalian methyl histone writer and eraser *in vivo*. Interplay of opposing chromatin-
432 modifying enzymes has been characterized in several biological processes and species.
433 For example, DNMT3A DNA methyltransferase and TET2 dioxigenase, which oppose
434 over DNA CpG methylation, can both counteract and cooperate to regulate gene
435 expression in hematopoietic stem cells (35). Set1 and Jhd2, the sole H3K4me writer-
436 eraser pair in yeast, have been shown to co-regulate transcription (36). However, a
437 fundamental question remained — is there any specific writer-eraser pairing in highly
438 duplicated gene families for a single chromatin modification? Mishra et al. showed that
439 KDM5A antagonizes KMT2A, KMT2B, and KMT2D to modulate the transient site-
440 specific DNA copy number gains in immortalized human cells (37). Cao et al. found that
441 failed differentiation of mouse embryonic stem cells due to *Kmt2d* deletion can be
442 rescued by *Kdm1a* knockdown (38). These pioneering efforts identified functional
443 interplay between the opposing enzymes *in vitro*; however, no *in vivo* study has been

444 reported. Thus, the present study substantially advances our understanding of how
445 methyl-histone enzymes functionally interact.
446
447 Brain development is particularly relevant to the H3K4me dynamics, because a cohort
448 of neurodevelopmental disorders has been genetically associated with impaired
449 functions of these enzymes, as discussed earlier. Unlike previous studies using
450 chemical approaches that block multiple chromatin regulators (13-15), we demonstrated
451 that manipulation of a single enzyme, KMT2A or KDM5C, is sufficient to reverse many
452 neurological traits in both of the two single-mutant models. This study motivates
453 interrogations of human populations to test if damaging mutations in writer and eraser
454 enzymes can coincide in unaffected individuals. Our work also opens a new avenue for
455 future studies to delineate the full interplay between the H3K4me-regulatory enzymes.
456
457 Several challenges remain, especially in linking molecular functions of KMT2A and
458 KDM5C to cellular and behavioral outcomes. First, we measured gene expression and
459 H3K4me3 in adult brain tissues, a mixture of many neuron and glia types, which may
460 mask potentially important molecular changes. Increasing spatiotemporal resolution of
461 the molecular study is an important future direction. Second, histone modifying
462 enzymes, including KDM5C, can exert non-enzymatic function (11, 39). Although it has
463 not been reported, there might be a non-histone substrate for KMT2A and KDM5C, as
464 shown in other histone modifying enzymes (12). Thus, our study does not rule out the
465 impact of these non-canonical roles of the two enzymes. Finally, in a fly model of
466 KMD5-intellctual disability (40, 41), impaired intestinal barrier and the altered microbiota

contribute to abnormal social behavior, pointing to a non-tissue-autonomous mechanism (42). Future studies are warranted to isolate the causal events for observed rescue effects. The first step would be to test the functional contribution of candidate genes, many of which encode peptide-hormone signaling factors (Table 1).

Increased social dominance is a novel behavioral trait we observed in both WDSTS and MRXSCJ mouse models. The amygdala is well known to mediate social behaviors. For example, lesions of BLA result in decreased aggression-like behavior and increased social interactions, and changes in transcriptional regulation in BLA are observed after social interactions (43). The dorsal hippocampus CA1 is a direct recipient region of BLA inputs (26). Decreased BLA and CA1 spine densities in *Kmt2a*-HET and *Kdm5c*-KO mice inversely correlate with increased social dominance and aggression (Figures 3 and 4). Together, these observations imply that decreased spine density is not a cause of increased social dominance, but rather reflects compensatory reduction of net synaptic strength due to increased excitation and/or a loss of inhibitory control in this circuit. Thus, determining the connectivity of the amygdala with other regions, including prelimbic, infralimbic, and orbitofrontal cortices as well as the ventral hippocampus, will be critical for understanding the changes in social behaviors in both WDSTS and MRXSCJ models.

It is important to note that the double mutations introduced in our mice were constitutive, and therefore a lifetime of adaptation to loss of these two major chromatin regulators may occur from early developmental stages. A more realistic therapeutic strategy may

be acute inhibition of KDM5C and KMT2A in the juvenile or mature brain. Previous work characterizing mouse models with excitatory-neuron specific ablation of *Kdm5c* or *Kmt2a* via *CamKII*-Cre found that conditional *Kmt2a* deletion led to clear learning deficits (20), while cognitive impairments in the conditional *Kdm5c*-KO mice were much milder than those of constitutive *Kdm5c*-KO mice (22). These results suggest a developmental origin of phenotypes in *Kdm5c*-KO. Future investigations are needed to address whether the effects of acute inhibition of opposing enzymes in these mouse models can restore such neurodevelopmental deficits.

Materials & methods

Statistics and Reproducibility

The proposed study was conducted with varied numbers of individual animals depending on the experiments. Data acquisition and analysis were conducted blindly except for molecular measurements including Western blots and genomics analyses. We did not remove any particular data points for their acquisition or analyses. Statistical tests were chosen based on the distribution of the data. Details of statistics and sampling are outlined below in each section.

Mouse

The *Kdm5c*-KO allele was previously described and maintained in C57BL/6J congenic background (21). *Kmt2a*-HET mice were generated by crossing previously described *Kmt2a*-flox (exons 8 and 9) mice with B6.129-Gt(ROSA)26Sor$^{tm1(cre/ERT2)Tyj}$/J-Cre mice (44). Our strategy was to use F1 hybrid for all studies as previously recommended as a

standard practice to eliminate deleterious homozygous mutations, which can result in abnormalities in the congenic lines, e.g. deafness in C57/BL6 (45). We backcrossed *Kmt2a*$^{+/-}$ mice onto the desired 129S1/SvImJ strain, by marker-assisted accelerated backcrossing through Charles River Labs. *Kmt2a*$^{+/-}$ mice were bred to the N4 generation at minimum, where mice were >99% congenic for 129S1/SvImJ. All experimental mice were generated as F1 generation hybrids from mating between 129S1/SvImJ *Kmt2a*$^{+/-}$ males and C57Bl/6 *Kdm5c*$^{+/-}$ females: WT males (*Kmt2a*$^{+/+}$, *Kdm5c*$^{+/y}$); *Kdm5c*-KO males (*Kmt2a*$^{+/+}$, *Kdm5c*$^{-/y}$); *Kmt2a*-HET males (*Kmt2a*$^{+/-}$, *Kdm5c*$^{+/y}$); and *Kdm5c-Kmt2a*-DM males (*Kmt2a*$^{+/-}$, *Kdm5c*$^{-/y}$). Genotypes were confirmed using the following primers: for *Kmt2a*, 5'-GCCAGTCAGTCCGAAAGTAC, 5'-AGGATGTTCAAAGTGCCTGC, 5'-GCTCTAGAACTAGTGGATCCC; for *Kdm5c*, 5'-CAGGTGGCTTACTGTGACATTGATG, 5'-TGGGTTTGAGGGATACTTTAGG, 5'-GGTTCTCAACACTCACATAGTG.

All mouse studies complied with the protocols (PRO00008568: Iwase and PRO00008807: Tronson) by the Institutional Animal Care & Use Committee (IACUC) of The University of Michigan.

Western blot analysis

Total proteins from adult brain tissues were subjected to Western blot analysis using in-house anti-KDM5C (21) and anti-GAPDH antibodies (G-9, Santa Cruz). For histone proteins, nuclei were enriched from the Dounce-homogenized brain tissues using Nuclei EZ prep Kit (Sigma, NUC-101). DNA were digested with micrococcal nuclease (MNase, NEB) for 10 minutes at room temperature, and total nuclear proteins were extracted by

boiling the samples with the SDS-PAGE sample buffer. The following antibodies were used for Western blot analyses: anti-H3K4me3 (Abcam, ab8580, 1:1000), anti-H3K4me2 (Thermo, #710796, 1:1000), anti-H3K4me1 (Abcam, ab8895, 1:1000), and anti-H3 C-terminus (Millipore, CS204377, 1:2000).

Brain histology

Mice were subjected to transcardial perfusion according to standard procedures. Fixed brains were sliced on a freeze microtome, yielding 30 μm sections that were then fixed, permeabilized, blocked, and stained with DAPI. Slides were imaged on an Olympus SZX16 microscope, with an Olympus U-HGLGPS fluorescence source and Q Imaging Retiga 6000 camera. Images were captured using Q-Capture Pro 7 software. Data were collected in a blind fashion, where samples were coded and genotypes only revealed after data collection was complete.

Behavioral paradigms

Prior to behavioral testing, mice were acclimated to the animal colony room for one week single-housing in standard cages provided with a lab diet and water *ad libitum*. A 12-hour light-dark cycle (7:00AM-7:00PM) was utilized with temperature and humidity maintained at 20 ±2 ºC and >30%, respectively. The University of Michigan Committee on the Use and Care of Animals approved all tests performed in this research. Five tests, listed in order of testing, were performed: Novel Object Recognition (five days), Context Fear Conditioning (two days), Three-Chambered Social Interaction (two days), Social Dominance Tube Test (three to four days), and Resident-Intruder (two to three

559 days). All testing was conducted in the morning by experimenters blind to genotype.
560 The cleaning agent used in every test between each trial was 70% ethanol. Data were
561 collected in a blind fashion, where mice were coded and genotypes were only revealed
562 after testing was complete.
563
564 *Contextual Fear Conditioning:* Mice were placed into a distinct context with white walls
565 (9 ¾ × 12 ¾ × 9 ¾ in) and a 36 steel rod grid floor (1/8 in diameter; ¼ spaced apart)
566 (Med-Associates, St. Albans, VT) and allowed to explore for three minutes, followed by
567 a two-second 0.8 mA shock, after which mice were immediately returned to their home
568 cages in the colony room. Twenty-four hours later, mice were returned to the context
569 and freezing behavior was assessed with NIR camera (VID-CAM-MONO-2A) and
570 VideoFreeze (MedAssociates, St Albans, VT). Freezing levels were compared between
571 genotypes using a between-groups analysis (one-way ANCOVA) with genotype as the
572 between-subjects factor, and "cohort" as the covariate, to reduce variability as a result
573 of multiple cohorts. Planned comparisons between genotypes were conducted, with
574 Bonferroni correction for multiple comparisons.
575
576 *Novel Object Recognition:* Mice were first habituated to testing arenas (40 x 30 x 32.5
577 cm^3) in three, 10-minute sessions over six consecutive days. Twenty-four hours later,
578 mice were allowed to explore two identical objects (a jar or egg, counterbalanced across
579 animals) for two, 10-minute trials spaced three hours apart. All animals were returned to
580 the arena, tested 24 hours after the first training session, and presented with one
581 training object ("familiar" object: jar or egg) and one "novel" object (egg or jar).

582 Exploration of the objects was defined as nose-point (sniffing) within 2 cm of the object.
583 Behavior was automatically measured by Ethovision XT9 software using a Euresys
584 Picolo U4H.264No/0 camera (Noldus, Cincinnati, OH). Preference was calculated as
585 the time spent exploring novel object/total time exploring both objects. One-sample
586 Wilcoxon signed-rank tests against 50% (no preference) was used to establish whether
587 animals remembered the original objects.
588
589
590 *Three-Chambered Social Interaction:* Mice were placed into a three-chambered
591 apparatus consisting of one central chamber (24 x 20 x 30 cm^3) and two identical side
592 chambers (24.5 x 20 x 30 cm^3) each with a containment enclosure (8 cm diameter; 18
593 cm height; grey stainless steel grid 3 mm diameter spaced 7.4 mm apart) and allowed
594 to habituate for 10 minutes. Twenty-four hours later, mice were returned to the
595 apparatus that now included a 2-3 month-old stranger male mouse (C57BL/6N) on one
596 side of the box (“stranger”), and a toy mouse approximately the same size and color as
597 the stranger mouse on the other (“toy”). Exploration of either the stranger or toy was
598 defined as nose-point (sniffing) within 2 cm of the enclosure and used as a measure of
599 social interaction. Behavior was automatically scored by Ethovision XT9 software as
600 described above, and social preference was defined as time exploring stranger/total
601 time spent exploring (stranger + toy). One-sample Wilcoxon signed-rank tests against
602 50% (no preference) was used to establish whether animals remembered the original
603 objects. Differences between genotypes were analyzed using an ANCOVA with cohort

as a covariate. Planned comparisons with Bonferroni correction for multiple comparisons were used to assess differences between genotypes.

Social Dominance Tube Test: Twenty-four hours prior to testing, mice were habituated to a plastic clear cylindrical tube (1.5 in diameter; 50 cm length) for 10 minutes. During the test, two mice of different genotypes were placed at opposite ends of the tube and allowed to walk to the middle. The match concluded when the one mouse (the dominant mouse) forced the other mouse (the submissive mouse) to retreat with all four paws outside of the tube (a “win” for the dominant mouse). Each mouse underwent a total of three matches against three different opponents for counterbalancing. Videos were recorded by Ethovision XT9 software as described above, and videos were manually scored by trained experimenters blind to genotype. The number of “wins” was reported as a percentage of total number of matches. Data were analyzed using an Exact Binomial Test with 0.5 as the probability of success (win or loss).

Resident-Intruder Aggression: Resident-intruder tests were used to assess aggression. Tests were performed on consecutive days, where the resident mouse was exposed to an unfamiliar intruder mouse for 15 minutes. A trial was terminated prematurely if blood was drawn, if an attack lasted continuously for 30 seconds, or if an intruder showed visible signs of injury after an attack. Resident mice were assessed for active aggression (darting, mounting, chasing/following, tail rattling, and boxing/parrying), as well as submissive behaviors (cowering, upright, running away). Intruder mice were assessed for passive defense (freezing, cowering, and digging). Behavior was recorded

and videos scored manually by experimenters blind to genotype. A repeated measures analysis, with cohort as a covariate, was used for each aggressive (genotype x aggression measures ANOVA) and submissive behavior (genotype x submissive) to analyze aggressive behaviors. Planned comparisons for genotype, with Bonferroni corrections for multiple comparisons were used to further analyze specific effects of genotype.

Neuronal Golgi staining and morphological analyses

Brains from adult (2-8 months) mice were dissected and incubated in a modified Golgi-Cox solution for two weeks at room temperature. The remaining procedure of Golgi immersion, cryosectioning, staining and coverslipping was performed as described previously (21). Four animals were used for each genotype, and pyramidal neurons in the basolateral amygdala and dorsal hippocampus CA1 per animal were quantified: N=24 neurons for WT, *Kmt2a*-HET and *Kdm5c*-KO, and N=27 neurons for DM. Quantification was done using commercially available software, NeuroLucida (v10, Microbrightfield, VT), installed on a Dell PC workstation that controlled a Zeiss Axioplan microscope with a CCD camera (1600 x 1200 pixels) and with a motorized X, Y, and Z focus for high-resolution image acquisition (100X oil immersion) and quantifications. The morphological analyses included: dendritic lengths, spine counts, and spine subtype morphology. All sample genotypes were blinded to the analysts throughout the course of the analysis.

649 The criteria for selecting candidate neurons for analysis were based on: (1) visualization
650 of a completely filled soma with no overlap of neighboring soma and completely filled
651 dendrites, (2) the tapering of most distal dendrites; and (3) the visualization of the
652 complete 3-D profile of dendritic trees using the 3-D display of the imaging software.
653
654 For quantitative analysis of spine subtypes (thin, stubby, mushroom, filopodia, and
655 branched spines), only spines orthogonal to the dendritic shaft were included in this
656 analysis, whereas spines protruding above or beneath the dendritic shaft were not
657 sampled. This principle remained consistent throughout the course of analysis.
658
659 After completion, the digital profile of neuron morphology was extrapolated and
660 transported to a multi-panel computer workstation, then quantitated using
661 NeuroExplorer program (Microbrightfield, VT), followed by statistical analysis (one- and
662 two-way ANOVAs, $p < 0.05$).
663
664 *RNA-seq*
665 Brains from adult (4.5 to 8 months) male mice were microdissected to obtain the
666 amygdala and hippocampus from Bregma ~ 4.80 mm regions. N=4 animals were used
667 per genotype. The ages of mice used for genomics study, RNA-seq and ChIP-seq, are
668 summarized in Supplementary Data 3. Tissue was homogenized in Tri Reagent
669 (Sigma). Samples were subjected to total RNA isolation, and RNA was purified using
670 RNEasy Mini Kit (Qiagen). ERCC spike-in RNA was added at this stage, according to
671 manufacturer's instructions (Life Technologies). Libraries were prepared using the

NEBNext® Ultra™ II Directional RNA Library Prep Kit with oligo-dT priming. Multiplexed libraries were pooled in approximately equimolar ratios and purified using Agencourt RNAClean XP beads (Beckman Coulter).

Libraries were sequenced on the Illumina Novaseq 6000 platform, with paired-end 150 base pair reads (24-35 million reads/library), according to standard procedures. Reads were mapped to the mm10 mouse genome (Gencode) using STAR (v2.5.3a), where only uniquely mapped reads were used for downstream analyses. Duplicates were removed by STAR, and a counts file was generated using FeatureCounts (Subread v1.5.0). BAM files were converted to bigwigs using deeptools (v3.1.3). Differentially expressed (DE) genes were called using DESeq2 (v1.14.1). Data analyses were performed with RStudio (v1.0.136). Fold change heatmaps was created using gplots heatmap.2 function.

To validate the microdissection of hippocampus and amygdala, we compared our RNA-seq datasets with similar RNA-seq data from Arbeitman (27) datasets, which involved the cerebellum, cortex, hippocampus, and amygdala. Briefly, count data underwent variance stabilizing transformation via DEseq2 vst function and Euclidean distances of the transformed values were calculated by dist command and the heatmap was generated by the pheatmap function. Linear regression analysis was performed using the smtr v3.4-8 slope.test function with intercept = FALSE and robust=FALSE options. Rescue-driving genes were chosen as genes that satisfy two conditions using R, **1)** abs (log2FC (single mutant vs DM) > 2, **2)** abs (log2FC (DM vs WT) < 0.7.

ChIP-seq

Amygdala tissues were microdissected from adult (8-14.5 months) male mice. N=2 animals were used for WT, and N=3 animals were used for *Kmt2a*-HET, *Kdm5c*-KO, and DM as biological replicates. Nuclei were isolated using a Nuclei EZ prep Kit (Sigma, NUC-101), and counted after Trypan blue staining. Approximately 20,000 nuclei for each replicate were subjected to MNase digestion as previously described (46). We essentially followed the native ChIP-seq protocol (46) with two modifications. One was to use a kit to generate sequencing libraries in one-tube reactions (NEB, E7103S). Another modification was to spike-in the panel of synthetic nucleosomes carrying major histone methylations (EpiCypher, SKU: 19-1001) (34). For ChIP, we used the rabbit monoclonal H3K4me3 antibody (Thermo, clone #RM340, 2 μg).

Libraries were sequenced on the Illumina NextSeq 500 platform, with single-end 75 base-pair sequencing, according to standard procedures. We obtained 20-59 million reads per sample. Reads were aligned to the mm10 mouse genome (Gencode) and a custom genome containing the sequences from our standardized, synthetic nucleosomes (EpiCypher) for normalization, using Bowtie allowing up to two mismatches. Only uniquely mapped reads were used for analysis. The range of uniquely mapped reads for input samples was 38-44 million reads. All IP replicates had a mean of 9.1 million uniquely mapped reads (range: 7.4-13.9 million). The enrichment of mapped synthetic spike-in nucleosomes compared to input was calculated and used as a normalization coefficient for read depth of each ChIP-seq replicate.

718

719 Peaks were called using MACS2 software (v 2.1.0.20140616) using input BAM files for
720 normalization, with filters for a q-value < 0.1 and a fold enrichment greater than 1.
721 Common peak sets were obtained via DiffBind, and count tables for the common peaks
722 were generated with the Bedtools multicov command. We removed “black-list” regions
723 that often give aberrant signals. Resulting count tables were piped into DEseq2 to
724 identify DMRs incorporating the synthetic nucleosome normalization into the read depth
725 factor. We used ChIPseeker to annotate H3K4me3 peaks with genomic features
726 including mm10 promoters (defined here as ±1 kb from annotated transcription start site
727 [TSS]). Normalized bam files were converted to bigwigs for visualization in the UCSC
728 genome browser. Genes near peaks were identified by ChIPseeker. RNA-seq and
729 ChIP-seq data were integrated using standard R commands and rescued amygdala
730 DEGs were chosen as genes that meet two criteria, **1)** abs (log2FC (single mutant vs
731 DM) > 1, **2)** abs (log2FC (DM vs WT) < 0.7. All scripts used in this study are available
732 upon request.

733

734 **Data Availability**

735 The RNA-seq and ChIP-seq are available in NCBI’s Gene Expression Omnibus (47).
736 Accession numbers are GSE127722 for RNA-seq, GSE127817 for ChIP-seq and
737 GSE127818 for SuperSeries.

738

739 **Acknowledgements**

We thank Dr. Ken Kwan, Mandy Lam, and Own Funk for their assistance with the RNA-seq library preparation protocol and use of their microscope; Chris Gates for his assistance with RNA-seq analyses; and Clara Farrehi, Jordan Rich, and Demetri Tsirukis for their assistance with experiments for transcriptome analyses, global histone methylation Western blots, and brain histology, respectively. We also thank Drs. Sally Camper, Stephen Parker, Stephanie Bielas, and Michael-Christopher Keogh, as well as the members of the Iwase and Bielas labs, for helpful discussions and critical review of the data. This work was funded by an NIH National Research Service Award T32-GM07544 (University of Michigan Predoctoral Genetics Training Program) from the National Institute of General Medicine Sciences (to CNV), an NIH National Research Service Award T32-HD079342 (University of Michigan Predoctoral Career Training in the Reproductive Sciences Program) from the National Institute of Child Health and Human Development (NICHD) (to CNV), University of Michigan Rackham Predoctoral Research Grants (to CNV), a Michigan Institute for Clinical and Health Research fellowship (Translational Research Education Certificate, supported by UL1TR000433 and UL1TR002240) (to CNV), a University of Michigan Rackham Predoctoral Fellowship award (to CNV), an Autism Science Foundation Predoctoral Fellowship award (to CNV), an NIH National Research Service Award. F31NS103377 from the National Institute of Neurological Disease & Stroke (NINDS) (to RSP), NIH NINDS Awards (R01NS089896 and R21NS104774) (to SI), Basil O'Connor Starter Scholar Research Awards from March of Dimes Foundation (to SI), and a Farrehi Family Foundation Grant (to SI).

Conflict of interest

MCW is CEO of Neurodigitech, LLC. The other authors declare no conflict of interest.

Author contributions

CNV, NCT, and SI conceived the study and designed the experiments. BR and KMC performed the mouse behavioral tests under the guidance of NCT. MCW oversaw dendritic morphometry analyses. CNV, KMB, PMG, and SI analyzed RNA-seq data. YAS performed global H3K4me3 analyses. RSP and SI performed H3K4me3 ChIP-seq and analyses. CNV performed the rest of experiments and analyses. YD and CEK provided key experimental recourse and made important intellectual contributions. CNV, MCW, RSP, CEK, NCT, and SI wrote and edited the manuscript.

Figures and Legends

Figure 1. The H3K4 methylopathies and generation of the *Kmt2a-Kdm5c* double-mutant (DM) mouse. (A) Histone H3 lysine 4 (H3K4me) methyltransferases (writers) and demethylases (erasers) depicted by their ability to place or remove H3K4me. Reader proteins recognizing specific H3K4me substrates (arrows) are depicted below. Genes are listed next to their associated neurodevelopmental disorder. KMT2A and KDM5C are highlighted in purple and green, respectively. WDSTS: Weideman-Steiner Syndrome; ID: intellectual disability; ASD: autism spectrum disorder, CPRF: cleft palate, psychomotor retardation, and distinctive facial features; ARID: autosomal recessive ID; MRXSCJ: mental retardation, X-linked, syndromic, Claes-Jensen type. **(B)** Mouse breeding scheme crossing congenic 129S1/SvImJ *Kmt2a*-heterozygous males with congenic C57/Bl6 *Kdm5c*-heterozygous females, resulting in F1 generation mice. Only males were used in this study. **(C)** Numbers of male offspring across 30 litters, showing Mendelian ratios of expected genotypes. **(D)** Left panel: Body weight of adult mice > 2 months of age (mean ± SEM, ****$p < 0.0001$ in one-way ANOVA). Right panel: Difference between group means of weight (mean ± 95% confidence intervals, *$p<0.05$, **$p<0.01$, ***$p<0.001$, ****$p<0.0001$ in Tukey's multiple comparison test).

Figure 2. Deficit of memory-related behavior in *Kdm5c*-KO and its rescue in DM. **(A)** Contextual fear conditioning test. Left panel: Freezing levels after shock on test day (mean ± SEM, *$p < 0.05$). Right panel: Difference between group means of freezing (mean ± 95% confidence intervals, *$p < 0.05$). **(B)** Novel object recognition test. Left panel: Preference for novel versus familiar object (mean ± SEM, *$p < 0.05$). Right panel:

Difference between group means of freeze response (mean ± 95% confidence intervals, *p<0.05). **(C)** Response to mild foot-shock (mean ± 95% confidence intervals, no statistical significance [n.s.],). **(D)** Locomotor activity (mean ± 95% confidence intervals, no statistical significance [n.s.]). N=21 WT, N=16 *Kmt2a*-HET, N=16 *Kdm5c*-KO, and N=12 DM animals were used for all studies.

Figure 3. Differential impacts of double mutation in social behavior. (A) Three chamber test for social interaction. Left panel: preference for stranger versus toy mouse (mean ± SEM, *p < 0.05). Right panel: Difference between group means of preference (mean ± 95% confidence intervals, *p<0.05). **(B)** Tube test for social dominance. Proportion of wins in matches of each mutant versus WT. Numbers on colored bars represent total number of wins for WT (grey, above) or each mutant (below) in every matchup. **p<0.01, ***p<0.001, Exact binomial test. **(C)** Resident intruder test. Left panel: average number of all aggressive and submissive behaviors (mean ± SEM, *p < 0.05, **p < 0.01). Right panel: Difference between group means of aggressive and submissive behaviors (mean ± 95% confidence intervals, *p < 0.05, **p < 0.01). N=21 WT, N=16 *Kmt2a*-HET, N=16 *Kdm5c*-KO, and N=12 DM animals were used for all studies.

Figure 4. Altered dendrite morphology of *Kdm5c*-KO and *Kmt2a*-HET was reversed in DM animals. (A) Representative images of basolateral amygdala (BLA) pyramidal neurons across all genotypes, depicting overall neuron morphology including dendrite lengths and dendritic spines. Scale bars represent: 100μm (above, whole

neuron image), 10μm (below, spine image). **(B and C)** Left panel: Total dendrite lengths **(B)** or spine density **(C)** (mean ± 95% *p<0.05, ****p<0.0001, one-way ANOVA). Right panel: Difference between group means (mean ± 95% confidence intervals, *p<0.05, **p<0.01, ***p<0.001, ****p<0.0001 in Tukey's multiple comparison test). **(D)** Quantification of spine morphology subtypes represented as percentage of total spines counted. **(E and F)** Morphometry of pyramidal neurons within the dorsal hippocampus CA1. At least 20 neurons from four animals per genotype were quantified for all panels.

Figure 5. The transcriptomes in the amygdala and hippocampus. (A) Number of differentially expressed (DE) genes across genotypes were determined using a threshold of *padj*-value < 0.1. or relaxed cut-off of p < 0.005 for *Kmt2a*-HET in **(B)** (see also Table S1). We analyzed amygdala and hippocampal tissues from four animals for each genotype. **(C)** Behavior of single-mutant DEGs in DM. Log2 fold change of DEGs relative to WT were plotted across the three mutants. Boxplot features: box, interquartile range (IQR); bold line, median; gray dots, individual genes. Associated p values result from Wilcoxon signed-rank tests. **(D)** Identification of rescue-driving genes and regression analysis. Blue fitting lines and slopes result from linear regression of log2 fold changes between the two genotypes. Gray shade: 95% confidence interval. *P*-values indicate probability of the null hypothesis that the fitting line does not differ from 1 (48). Red circles: rescue-driving genes (see method).

844 **Figure 6. Altered H3K4me3 landscapes in the amygdala and rescue effect in DM.**
845 **(A)** Western blot of whole brain lysates showing unchanged global H3K4 methylation
846 across genotypes. Total histone H3 was detected using an antibody recognizing the C-
847 terminus of H3, and used as a control for equal loading. **(B)** PCA analysis of H3K4me3
848 ChIPseq replicates. We analyzed amygdala tissue from 2 to 3 animals (rep1-3) for each
849 genotype (see Methods). **(C)** Number of H3K4me3 DMRs in 2a-HET, 5c-KO, or DM
850 compared to WT across the genome. 2A-HET DMRs are retrieved with a relaxed
851 threshold ($p < 0.05$). **(D)** Direction of H3K4me3 changes between single mutants.
852 Genes are colored based on the direction of misregulation between the single mutants.
853 **(E)** Behavior of single-mutant DMRs in DM. Log2 fold change of DMRs relative to WT
854 were plotted across the three mutants. Boxplot features: box, interquartile range (IQR);
855 bold line, median; gray dots, individual genes. Associated *p* values result from Wilcoxon
856 signed-rank tests. **(F)** Genomic features of H3K4me3 peaks. **(G)** Involvement of
857 H3K4me3 restoration near rescued DEGs. H3K4me3 log2 fold changes (FC) are plotted
858 as function of mRNA log2 FC between DM and single mutants. Red line: linear
859 regression fitting line with 95% confidence interval (gray shade). The gene numbers fall
860 into each of the four quadrants as indicated (Q1-Q4). Results (p) of χ^2 test and
861 Pearson's correlation coefficient (r) and p-value (p) are noted.
862

Gene symbol	Encoded protein	Chromosome	Description
Tacr1	Tachykinin receptor 1	chr6	Tachykinin receptor (aka neurokinin-1 or Substance-P receptor). G-protein coupled receptors found across the brain. Elevated *TACR1* mRNA levels in ASD patients with heightened aggression (49). Decreased aggression in *Tacr1*-KO mice (50).
Lhb	Beta subunit of luteinizing hormone (LH)	chr7	Major roles of LH in testosterone production. Additional roles of LH in learning and memory functions, e.g. elevated LH impairs spatial memory of rodents (51).
Trh	Thyrotropin-releasing hormone (TRH)	chr6	Primary TRH production in hypothalamic neurons. Some production and activity within the hippocampus. TRH stimulates GABA release within CA1 of the hippocampus (52).
Gabre	The epsilon subunit of the GABA-A	chrX	The epsilon subunit of GABA-A Receptor, an inhibitory chloride channel. Agonist-independent activity produces a tonic inhibitory tone onto neurons (53). Highest in the hypothalamus.
Adcy2	Adenylyl cyclase 2	chr13	Stimulated by G-protein signaling and PKC. High expression in the soma and dendrites of hippocampal neurons and a proposed role in coincidence detection (54).
Adora2a	Adenosine A2a receptor	chr10	A G-protein coupled receptor of extracellular adenosine. A regulator of neurogenesis and hippocampal volume. Modulatory roles of BDNF expression and GABA and glutamate signaling in the hippocampus (55). Increased body mass, anxiety, and heightened aggression in *Adora2a*-KO mice (56).
Pomc	Pro-opiomelanocortin	chr12	A peptide hormone regulating the hypothalamic function such as feeding. High expression in the hypothalamus, and lower expression in the amygdala and hippocampus. Implicated in the cognitive decline of Alzheimer's disease (31).
Mc3r	Melanocortin 3 receptor	chr2	MC3R is receptor for cleavage products of POMC. The hypothalamic function in weight and feeding. Roles in hippocampal memory consolidation (33).
Agt	Angiotensinogen	chr8	A peptide hormone primarily produced by astrocytes and converted into Angiotensin, neuroactive peptides. Well-known roles in vascular regulation, such as blood pressure. Angiotensin II inhibits LTP in the dentate gyrus in the hippocampus (57).
P2ry14	Purinergic receptor P2Y, G-protein coupled	chr3	G-protein coupled receptor that binds UDP-glucose.

Table 1. Rescued 5C-DEGs that drove enrichment of the KEGG pathway "Neuroactive ligand-receptor interaction"

865 **References**

866

867 1. Faundes V, Newman WG, Bernardini L, Canham N, Clayton-Smith J, Dallapiccola B, et
868 al. Histone Lysine Methylases and Demethylases in the Landscape of Human
869 Developmental Disorders. *Am J Hum Genet.* 2018;102(1):175-87.
870 2. Kouzarides T. Chromatin modifications and their function. *Cell.* 2007;128(4):693-
871 705.
872 3. Iwase S, and Shi Y. Histone and DNA modifications in mental retardation. *Progress in*
873 *drug research Fortschritte der Arzneimittelforschung Progres des recherches*
874 *pharmaceutiques.* 2011;67:147-73.
875 4. Barski A, Cuddapah S, Cui K, Roh TY, Schones DE, Wang Z, et al. High-resolution
876 profiling of histone methylations in the human genome. *Cell.* 2007;129(4):823-37.
877 5. Heintzman ND, Stuart RK, Hon G, Fu Y, Ching CW, Hawkins RD, et al. Distinct and
878 predictive chromatin signatures of transcriptional promoters and enhancers in the
879 human genome. *Nature genetics.* 2007;39(3):311-8.
880 6. Vermeulen M, Mulder KW, Denissov S, Pijnappel WW, van Schaik FM, Varier RA, et
881 al. Selective anchoring of TFIID to nucleosomes by trimethylation of histone H3
882 lysine 4. *Cell.* 2007;131(1):58-69.
883 7. Lauberth SM, Nakayama T, Wu X, Ferris AL, Tang Z, Hughes SH, et al. H3K4me3
884 Interactions with TAF3 Regulate Preinitiation Complex Assembly and Selective Gene
885 Activation. *Cell.* 2013;152(5):1021-36.
886 8. Local A, Huang H, Albuquerque CP, Singh N, Lee AY, Wang W, et al. Identification of
887 H3K4me1-associated proteins at mammalian enhancers. *Nature genetics.*
888 2018;50(1):73-82.
889 9. Allis CD, Berger SL, Cote J, Dent S, Jenuwien T, Kouzarides T, et al. New
890 nomenclature for chromatin-modifying enzymes. *Cell.* 2007;131(4):633-6.
891 10. Vallianatos CN, and Iwase S. Disrupted intricacy of histone H3K4 methylation in
892 neurodevelopmental disorders. *Epigenomics.* 2015;7(3):503-19.
893 11. Aubert Y, Egolf S, and Capell BC. The Unexpected Noncatalytic Roles of Histone
894 Modifiers in Development and Disease. *Trends Genet.* 2019;35(9):645-57.
895 12. Zhang X, Wen H, and Shi X. Lysine methylation: beyond histones. *Acta Biochim*
896 *Biophys Sin (Shanghai).* 2012;44(1):14-27.
897 13. Alarcon JM, Malleret G, Touzani K, Vronskaya S, Ishii S, Kandel ER, et al. Chromatin
898 acetylation, memory, and LTP are impaired in CBP+/- mice: a model for the
899 cognitive deficit in Rubinstein-Taybi syndrome and its amelioration. *Neuron.*
900 2004;42(6):947-59.
901 14. Bjornsson HT, Benjamin JS, Zhang L, Weissman J, Gerber EE, Chen YC, et al. Histone
902 deacetylase inhibition rescues structural and functional brain deficits in a mouse
903 model of Kabuki syndrome. *Science translational medicine.* 2014;6(256):256ra135.
904 15. Park J, Thomas S, and Munster PN. Epigenetic modulation with histone deacetylase
905 inhibitors in combination with immunotherapy. *Epigenomics.* 2015;7(4):641-52.
906 16. Jones WD, Dafou D, McEntagart M, Woollard WJ, Elmslie FV, Holder-Espinasse M, et
907 al. De Novo Mutations in MLL Cause Wiedemann-Steiner Syndrome. *American*
908 *Journal of Human Genetics.* 2012;91(2):358-64.

17. Jensen LR, Amende M, Gurok U, Moser B, Gimmel V, Tzschach A, et al. Mutations in the JARID1C gene, which is involved in transcriptional regulation and chromatin remodeling, cause X-linked mental retardation. *Am J Hum Genet.* 2005;76(2):227-36.
18. Gupta S, Kim SY, Artis S, Molfese DL, Schumacher A, Sweatt JD, et al. Histone methylation regulates memory formation. *J Neurosci.* 2010;30(10):3589-99.
19. Jakovcevski M, Ruan H, Shen EY, Dincer A, Javidfar B, Ma Q, et al. Neuronal Kmt2a/Mll1 histone methyltransferase is essential for prefrontal synaptic plasticity and working memory. *J Neurosci.* 2015;35(13):5097-108.
20. Kerimoglu C, Sakib MS, Jain G, Benito E, Burkhardt S, Capece V, et al. KMT2A and KMT2B Mediate Memory Function by Affecting Distinct Genomic Regions. *Cell Rep.* 2017;20(3):538-48.
21. Iwase S, Brookes E, Agarwal S, Badeaux AI, Ito H, Vallianatos CN, et al. A Mouse Model of X-linked Intellectual Disability Associated with Impaired Removal of Histone Methylation. *Cell Rep.* 2016.
22. Scandaglia M, Lopez-Atalaya JP, Medrano-Fernandez A, Lopez-Cascales MT, Del Blanco B, Lipinski M, et al. Loss of Kdm5c Causes Spurious Transcription and Prevents the Fine-Tuning of Activity-Regulated Enhancers in Neurons. *Cell Rep.* 2017;21(1):47-59.
23. Cao F, Townsend EC, Karatas H, Xu J, Li L, Lee S, et al. Targeting MLL1 H3K4 methyltransferase activity in mixed-lineage leukemia. *Mol Cell.* 2014;53(2):247-61.
24. Varholick JA, Bailoo JD, Palme R, and Würbel H. Phenotypic variability between Social Dominance Ranks in laboratory mice. *Sci Rep.* 2018;8(1):6593.
25. Penzes P, Cahill ME, Jones KA, VanLeeuwen JE, and Woolfrey KM. Dendritic spine pathology in neuropsychiatric disorders. *Nat Neurosci.* 2011;14(3):285-93.
26. Yang Y, and Wang JZ. From Structure to Behavior in Basolateral Amygdala-Hippocampus Circuits. *Front Neural Circuits.* 2017;11:86.
27. Arbeitman MN. Maternal Experience Leads to Lasting Gene Expression Changes in Some Regions of the Mouse Brain. *G3 (Bethesda).* 2019;9(8):2623-8.
28. Outchkourov NS, Muino JM, Kaufmann K, van Ijcken WF, Groot Koerkamp MJ, van Leenen D, et al. Balancing of histone H3K4 methylation states by the Kdm5c/SMCX histone demethylase modulates promoter and enhancer function. *Cell Rep.* 2013;3(4):1071-9.
29. Civelli O, Birnberg N, and Herbert E. Detection and quantitation of pro-opiomelanocortin mRNA in pituitary and brain tissues from different species. *J Biol Chem.* 1982;257(12):6783-7.
30. Pałasz A, Bandyszewska M, Rojczyk E, and Wiaderkiewicz R. Effect of extended olanzapine administration on POMC and neuropeptide Y mRNA levels in the male rat amygdala and hippocampus. *Pharmacol Rep.* 2016;68(2):292-6.
31. Shen Y, Tian M, Zheng Y, Gong F, Fu AKY, and Ip NY. Stimulation of the Hippocampal POMC/MC4R Circuit Alleviates Synaptic Plasticity Impairment in an Alzheimer's Disease Model. *Cell Rep.* 2016;17(7):1819-31.
32. Roselli-Rehfuss L, Mountjoy KG, Robbins LS, Mortrud MT, Low MJ, Tatro JB, et al. Identification of a receptor for gamma melanotropin and other proopiomelanocortin peptides in the hypothalamus and limbic system. *Proceedings of the National Academy of Sciences of the United States of America.* 1993;90(19):8856-60.

33. Machado I, González P, Schiöth HB, Lasaga M, and Scimonelli TN. α-Melanocyte-stimulating hormone (α-MSH) reverses impairment of memory reconsolidation induced by interleukin-1 beta (IL-1 beta) hippocampal infusions. *Peptides.* 2010;31(11):2141-4.
34. Shah RN, Grzybowski AT, Cornett EM, Johnstone AL, Dickson BM, Boone BA, et al. Examining the Roles of H3K4 Methylation States with Systematically Characterized Antibodies. *Mol Cell.* 2018;72(1):162-77 e7.
35. Zhang X, Su J, Jeong M, Ko M, Huang Y, Park HJ, et al. DNMT3A and TET2 compete and cooperate to repress lineage-specific transcription factors in hematopoietic stem cells. *Nature genetics.* 2016;48(9):1014-23.
36. Ramakrishnan S, Pokhrel S, Palani S, Pflueger C, Parnell TJ, Cairns BR, et al. Counteracting H3K4 methylation modulators Set1 and Jhd2 co-regulate chromatin dynamics and gene transcription. *Nat Commun.* 2016;7:11949.
37. Mishra S, Van Rechem C, Pal S, Clarke TL, Chakraborty D, Mahan SD, et al. Cross-talk between Lysine-Modifying Enzymes Controls Site-Specific DNA Amplifications. *Cell.* 2018;175(6):1716.
38. Cao K, Collings CK, Morgan MA, Marshall SA, Rendleman EJ, Ozark PA, et al. An Mll4/COMPASS-Lsd1 epigenetic axis governs enhancer function and pluripotency transition in embryonic stem cells. *Sci Adv.* 2018;4(1):eaap8747.
39. Vallianatos CN, Farrehi C, Friez MJ, Burmeister M, Keegan CE, and Iwase S. Altered Gene-Regulatory Function of KDM5C by a Novel Mutation Associated With Autism and Intellectual Disability. *Front Mol Neurosci.* 2018;11:104.
40. Liu X, and Secombe J. The Histone Demethylase KDM5 Activates Gene Expression by Recognizing Chromatin Context through Its PHD Reader Motif. *Cell Rep.* 2015;13(10):2219-31.
41. Zamurrad S, Hatch HAM, Drelon C, Belalcazar HM, and Secombe J. A Drosophila Model of Intellectual Disability Caused by Mutations in the Histone Demethylase KDM5. *Cell Rep.* 2018;22(9):2359-69.
42. Chen K, Luan X, Liu Q, Wang J, Chang X, Snijders AM, et al. Drosophila Histone Demethylase KDM5 Regulates Social Behavior through Immune Control and Gut Microbiota Maintenance. *Cell Host Microbe.* 2019;25(4):537-52 e8.
43. McCann KE, Sinkiewicz DM, Rosenhauer AM, Beach LQ, and Huhman KL. Transcriptomic Analysis Reveals Sex-Dependent Expression Patterns in the Basolateral Amygdala of Dominant and Subordinate Animals After Acute Social Conflict. *Mol Neurobiol.* 2018.
44. McMahon KA, Hiew SY, Hadjur S, Veiga-Fernandes H, Menzel U, Price AJ, et al. Mll has a critical role in fetal and adult hematopoietic stem cell self-renewal. *Cell Stem Cell.* 2007;1(3):338-45.
45. Silva AJ, Simpson EM, Takahashi JS, Lipp HP, Nakanishi S, Wehner JM, et al. Mutant mice and neuroscience: recommendations concerning genetic background. Banbury Conference on genetic background in mice. *Neuron.* 1997;19(4):755-9.
46. Brind'Amour J, Liu S, Hudson M, Chen C, Karimi MM, and Lorincz MC. An ultra-low-input native ChIP-seq protocol for genome-wide profiling of rare cell populations. *Nat Commun.* 2015;6:6033.

47. Edgar R, Domrachev M, and Lash AE. Gene Expression Omnibus: NCBI gene expression and hybridization array data repository. *Nucleic Acids Res.* 2002;30(1):207-10.
48. Warton DI, Wright IJ, Falster DS, and Westoby M. Bivariate line-fitting methods for allometry. *Biol Rev Camb Philos Soc.* 2006;81(2):259-91.
49. Sener EF, Taheri S, Sahin MC, Bayramov KK, Marasli MK, Zararsiz G, et al. Altered Global mRNA Expressions of Pain and Aggression Related Genes in the Blood of Children with Autism Spectrum Disorders. *J Mol Neurosci.* 2019;67(1):89-96.
50. De Felipe C, Herrero JF, O'Brien JA, Palmer JA, Doyle CA, Smith AJ, et al. Altered nociception, analgesia and aggression in mice lacking the receptor for substance P. *Nature.* 1998;392(6674):394-7.
51. Burnham V, Sundby C, Laman-Maharg A, and Thornton J. Luteinizing hormone acts at the hippocampus to dampen spatial memory. *Horm Behav.* 2017;89:55-63.
52. Deng PY, Porter JE, Shin HS, and Lei S. Thyrotropin-releasing hormone increases GABA release in rat hippocampus. *J Physiol.* 2006;577(Pt 2):497-511.
53. Neelands TR, Fisher JL, Bianchi M, and Macdonald RL. Spontaneous and gamma-aminobutyric acid (GABA)-activated GABA(A) receptor channels formed by epsilon subunit-containing isoforms. *Mol Pharmacol.* 1999;55(1):168-78.
54. Baker LP, Nielsen MD, Impey S, Hacker BM, Poser SW, Chan MY, et al. Regulation and immunohistochemical localization of betagamma-stimulated adenylyl cyclases in mouse hippocampus. *J Neurosci.* 1999;19(1):180-92.
55. Vaz SH, Lérias SR, Parreira S, Diógenes MJ, and Sebastião AM. Adenosine A2A receptor activation is determinant for BDNF actions upon GABA and glutamate release from rat hippocampal synaptosomes. *Purinergic Signal.* 2015;11(4):607-12.
56. Ledent C, Vaugeois JM, Schiffmann SN, Pedrazzini T, El Yacoubi M, Vanderhaeghen JJ, et al. Aggressiveness, hypoalgesia and high blood pressure in mice lacking the adenosine A2a receptor. *Nature.* 1997;388(6643):674-8.
57. Denny JB, Polan-Curtain J, Wayner MJ, and Armstrong DL. Angiotensin II blocks hippocampal long-term potentiation. *Brain Res.* 1991;567(2):321-4.

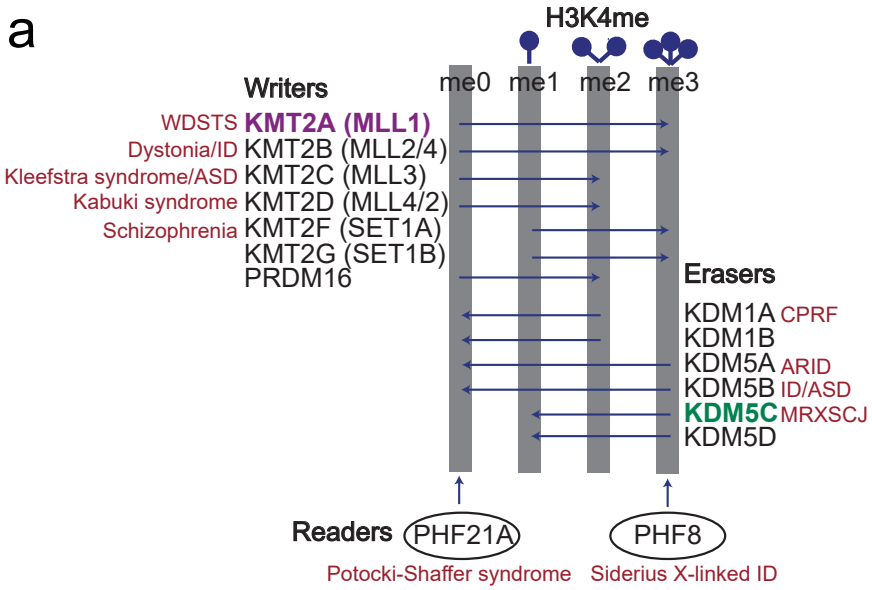

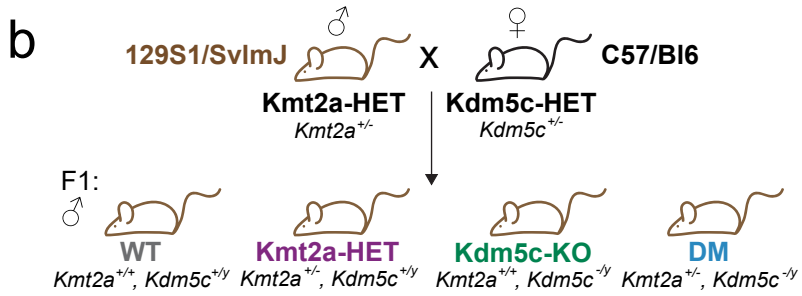

c

Number of offspring across 30 litters (% total males)			
WT	2a-HET	5c-KO	DM
17 (25%)	16 (23%)	21 (31%)	14 (21%)

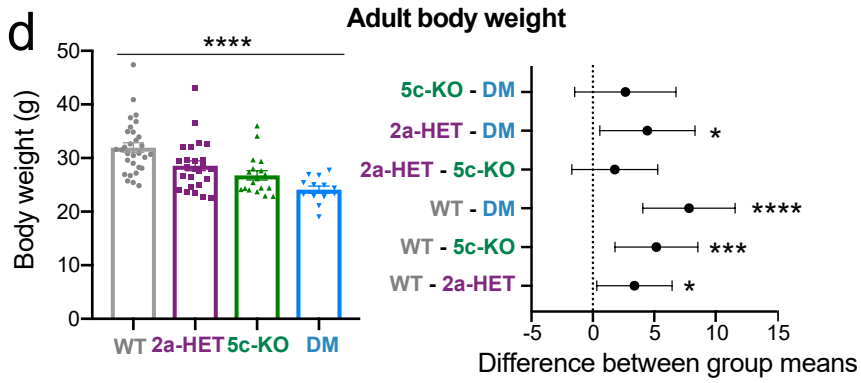

Figure 1

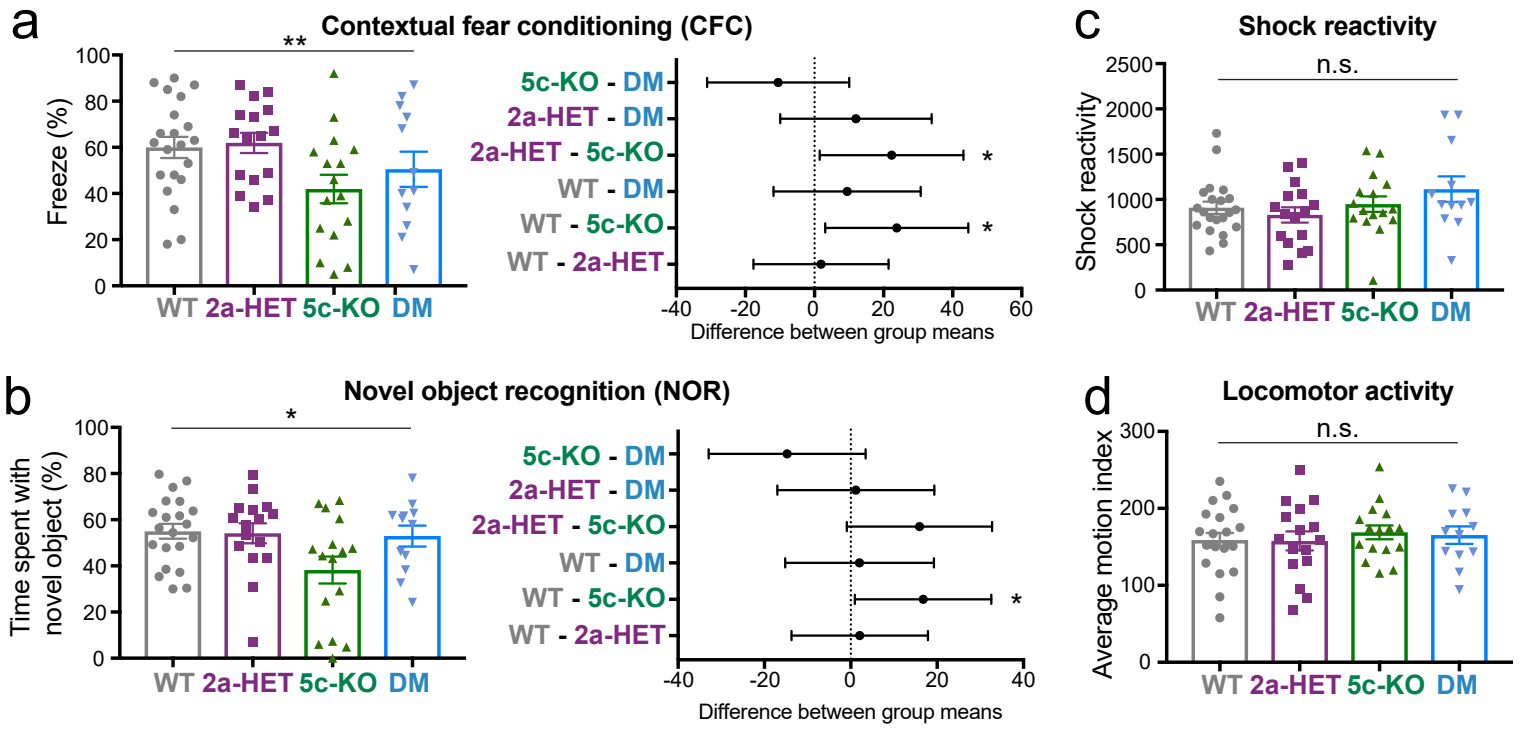

Figure 2

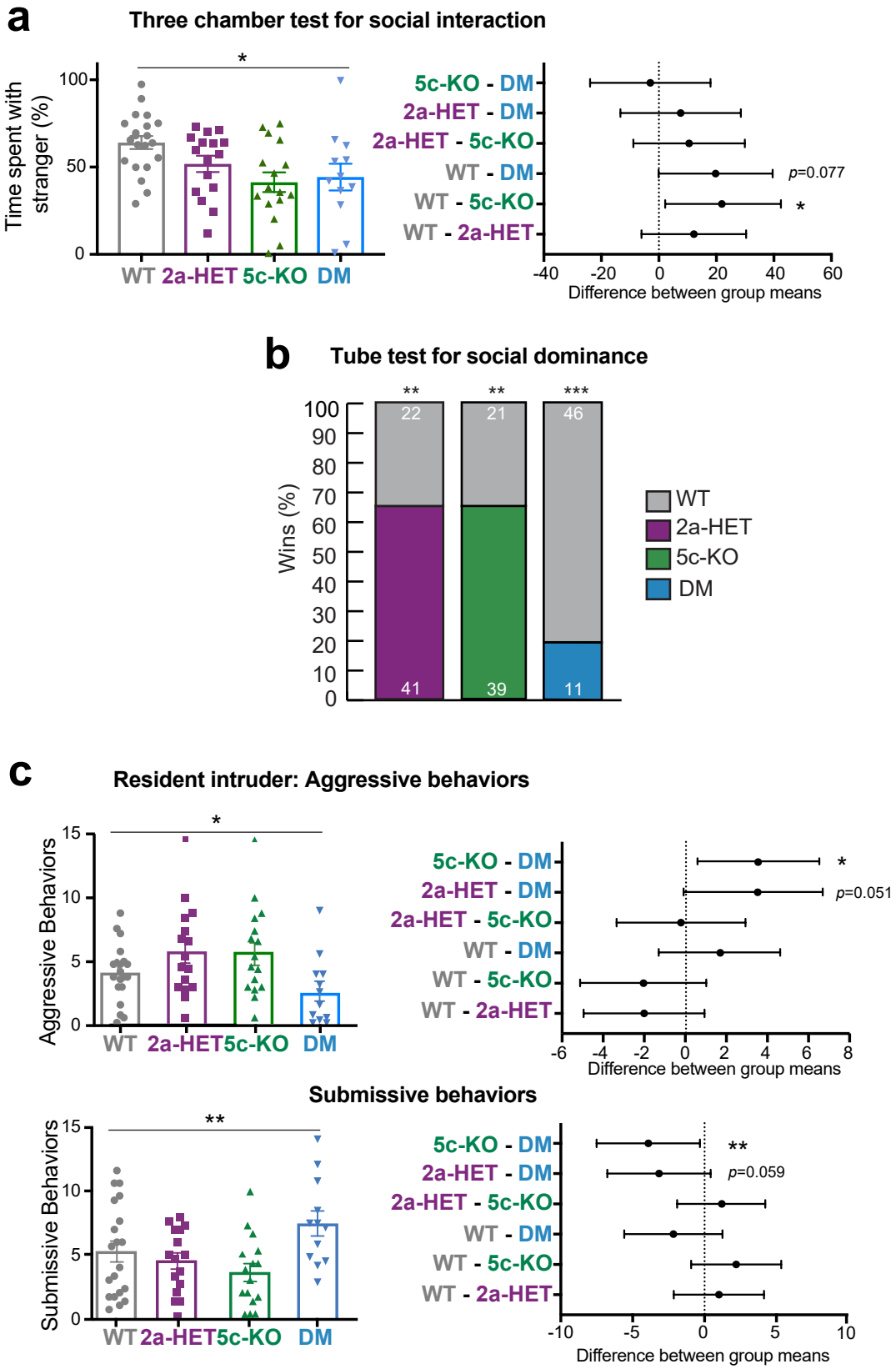

Figure 3

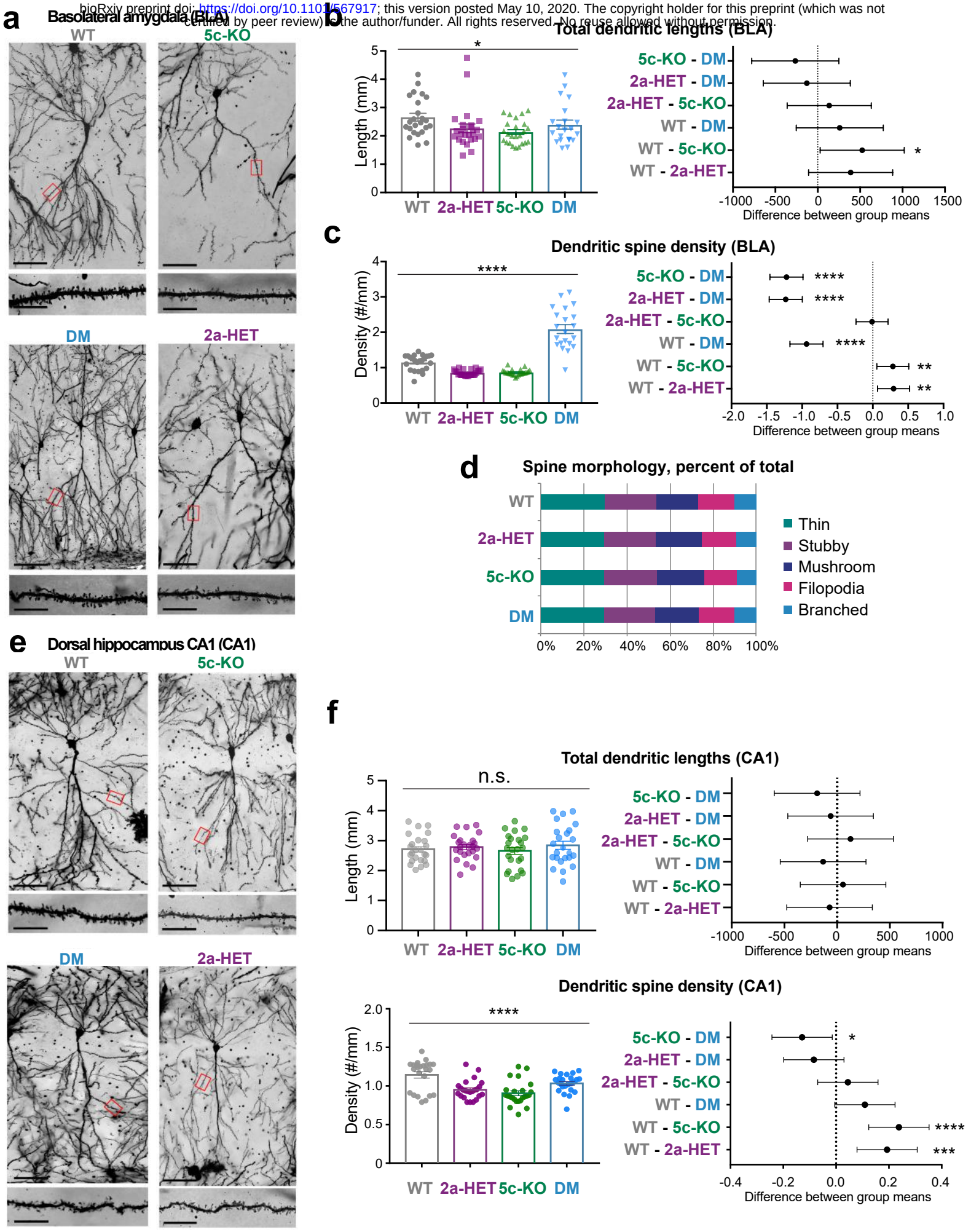

Figure 4

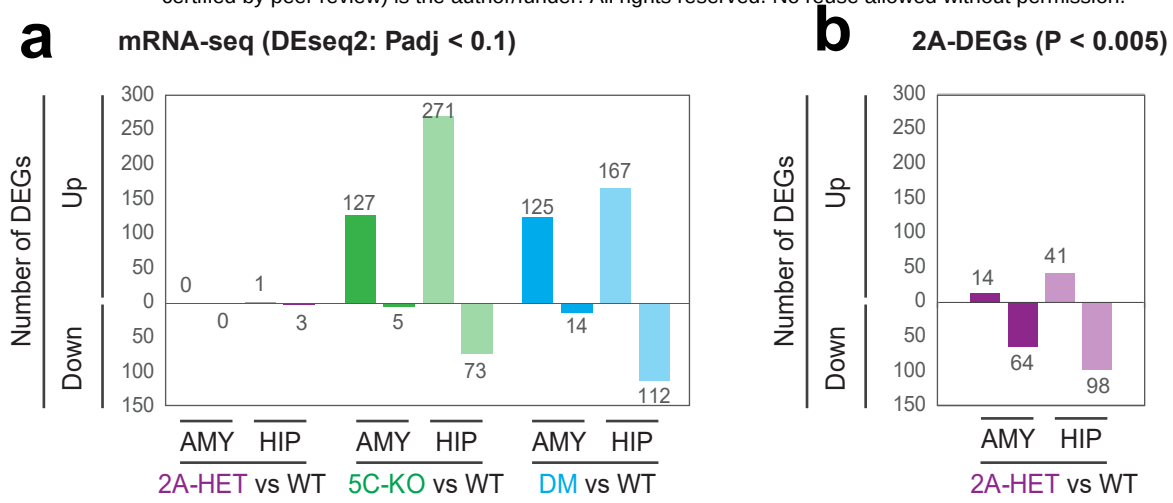

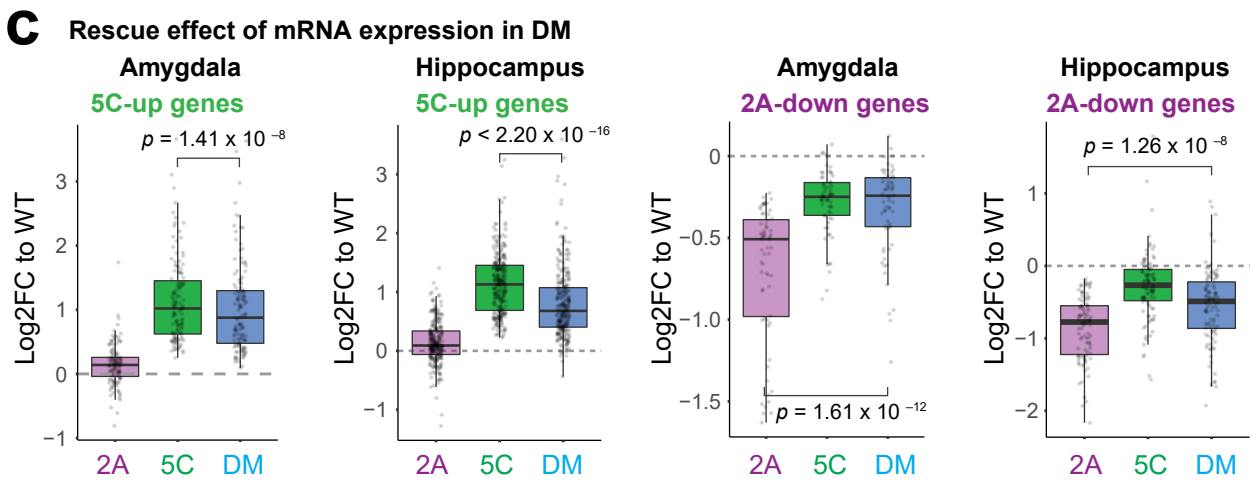

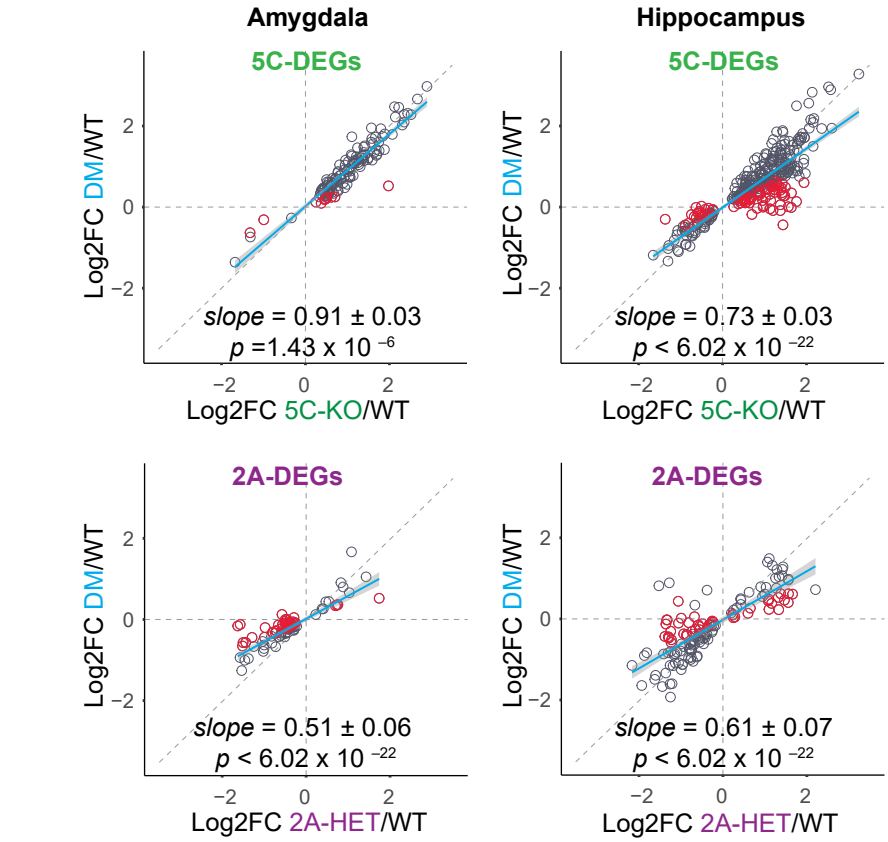

Figure 5

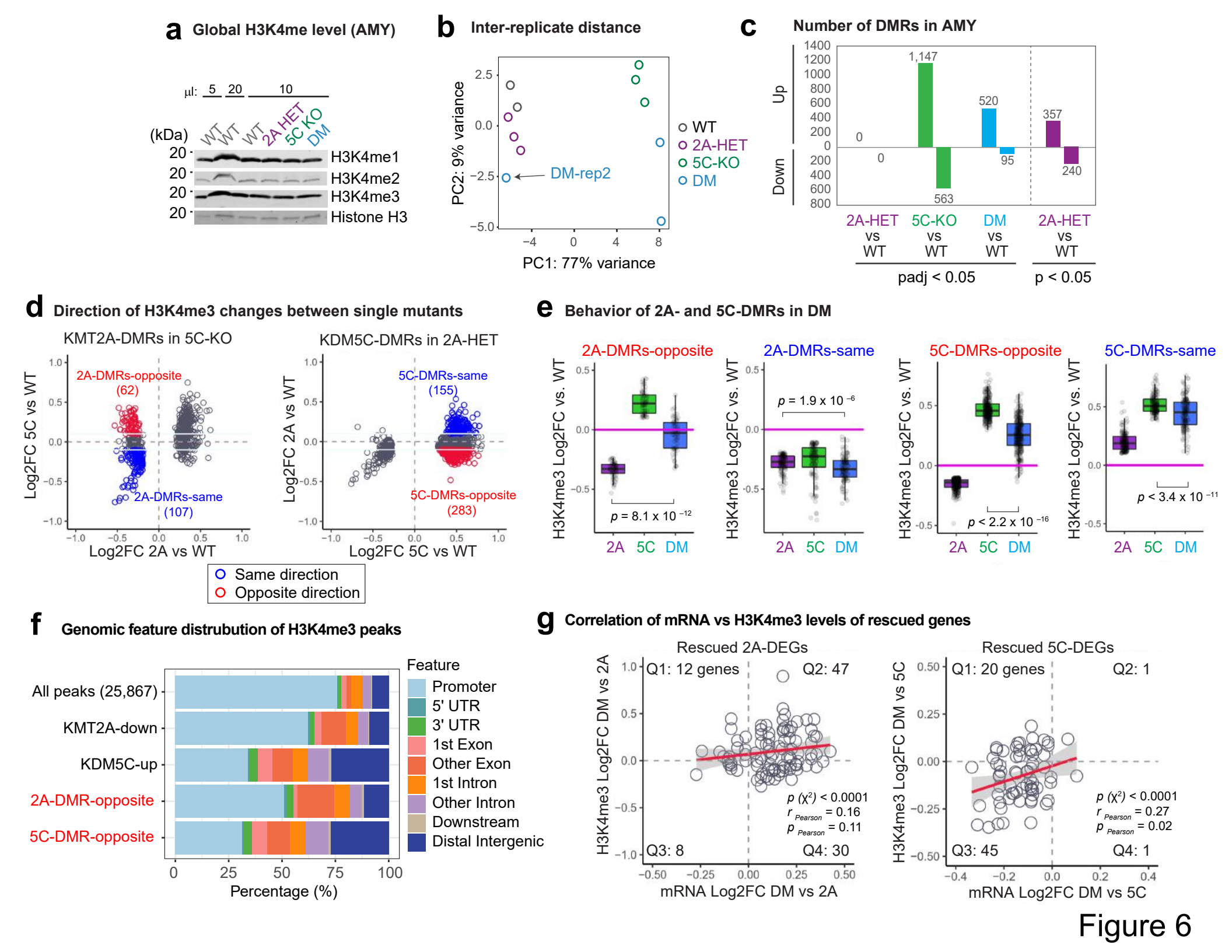
a
Global H3K4me level (AMY)
µl: 5 20 10
(kDa)
WT WT WT 2A HET 5C KO DM
20 H3K4me1
20 H3K4me2
20 H3K4me3
20 Histone H3
b
Inter-replicate distance
PC2: 9% variance
PC1: 77% variance
DM-rep2
WT
2A-HET
5C-KO
DM
c
Number of DMRs in AMY
Up
Down
1,147
520
357
0
0
95
563
240
2A-HET vs WT
5C-KO vs WT
DM vs WT
2A-HET vs WT
padj < 0.05
p < 0.05
d
Direction of H3K4me3 changes between single mutants
KMT2A-DMRs in 5C-KO
KDM5C-DMRs in 2A-HET
Log2FC 5C vs WT
Log2FC 2A vs WT
2A-DMRs-opposite (62)
2A-DMRs-same (107)
5C-DMRs-same (155)
5C-DMRs-opposite (283)
Log2FC 2A vs WT
Log2FC 5C vs WT
Same direction
Opposite direction
e
Behavior of 2A- and 5C-DMRs in DM
2A-DMRs-opposite
2A-DMRs-same
5C-DMRs-opposite
5C-DMRs-same
H3K4me3 Log2FC vs. WT
p = 8.1 x 10 −12
p = 1.9 x 10 −6
p < 2.2 x 10 −16
p < 3.4 x 10 −11
2A 5C DM
f
Genomic feature distrubution of H3K4me3 peaks
All peaks (25,867)
KMT2A-down
KDM5C-up
2A-DMR-opposite
5C-DMR-opposite
Percentage (%)
Feature
Promoter
5' UTR
3' UTR
1st Exon
Other Exon
1st Intron
Other Intron
Downstream
Distal Intergenic
g
Correlation of mRNA vs H3K4me3 levels of rescued genes
Rescued 2A-DEGs
Rescued 5C-DEGs
H3K4me3 Log2FC DM vs 2A
H3K4me3 Log2FC DM vs 5C
Q1: 12 genes
Q2: 47
Q3: 8
Q4: 30
Q1: 20 genes
Q2: 1
Q3: 45
Q4: 1
p (χ²) < 0.0001
r Pearson = 0.16
p Pearson = 0.11
p (χ²) < 0.0001
r Pearson = 0.27
p Pearson = 0.02
mRNA Log2FC DM vs 2A
mRNA Log2FC DM vs 5C

Figure 6

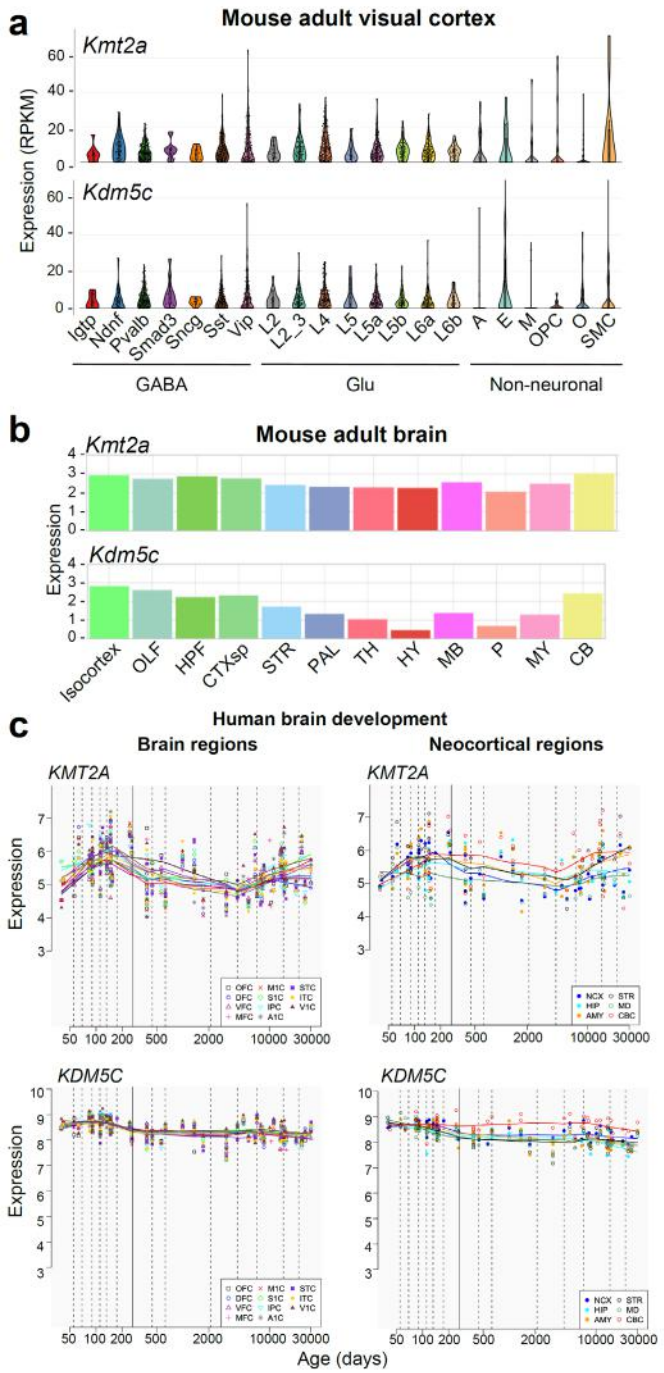

Supplementary Figure 1. Expression of KMT2A and KDM5C. (A) Expression of *Kmt2a* and *Kdm5c*, from FACS-sorted single cells of mouse visual cortex, shown in reads per kilobase of transcript per million mapped reads (RPKM). Neuronal cells: GABAergic (GABA), Glutamatergic (Glu). Non-neuronal cells: astrocytes (A); endothelial cells (E); microglia (M), oligodendrocyte precursor cells (OPC); oligodendrocytes (O); smooth muscle cells (SMC). Image credit: Broad Institute "Single Cell Portal" transcriptome of adult mouse visual cortex (1). **(B)** Expression of *Kmt2a* and *Kdm5c* mRNA from adult mouse brain, shown in log2 of raw expression value from *in situ* hybridization. Brain regions: Isocortex, olfactory areas (OLF), hippocampal formation (HPF), cortical subplate (CTXsp), striatum (STR), pallidum (PAL), thalamus (TH), hypothalamus (HY), midbrain (MB), pons (P), medulla (MY), cerebellum (CB). Image credit: Allen Institute, Allen Mouse Brain Atlas (2004) (2). **(C)** Expression of *KMT2A* and *KDM5C* transcripts, from developing and adult human brains, shown in RPKM. Human development and adulthood were split into the following Periods: 1-7 fetal development; 8-9 birth and infancy; 10-11 childhood; 12 adolescence; and 13-15 adulthood. Image credit: Human Brain Transcriptome Atlas (3, 4)

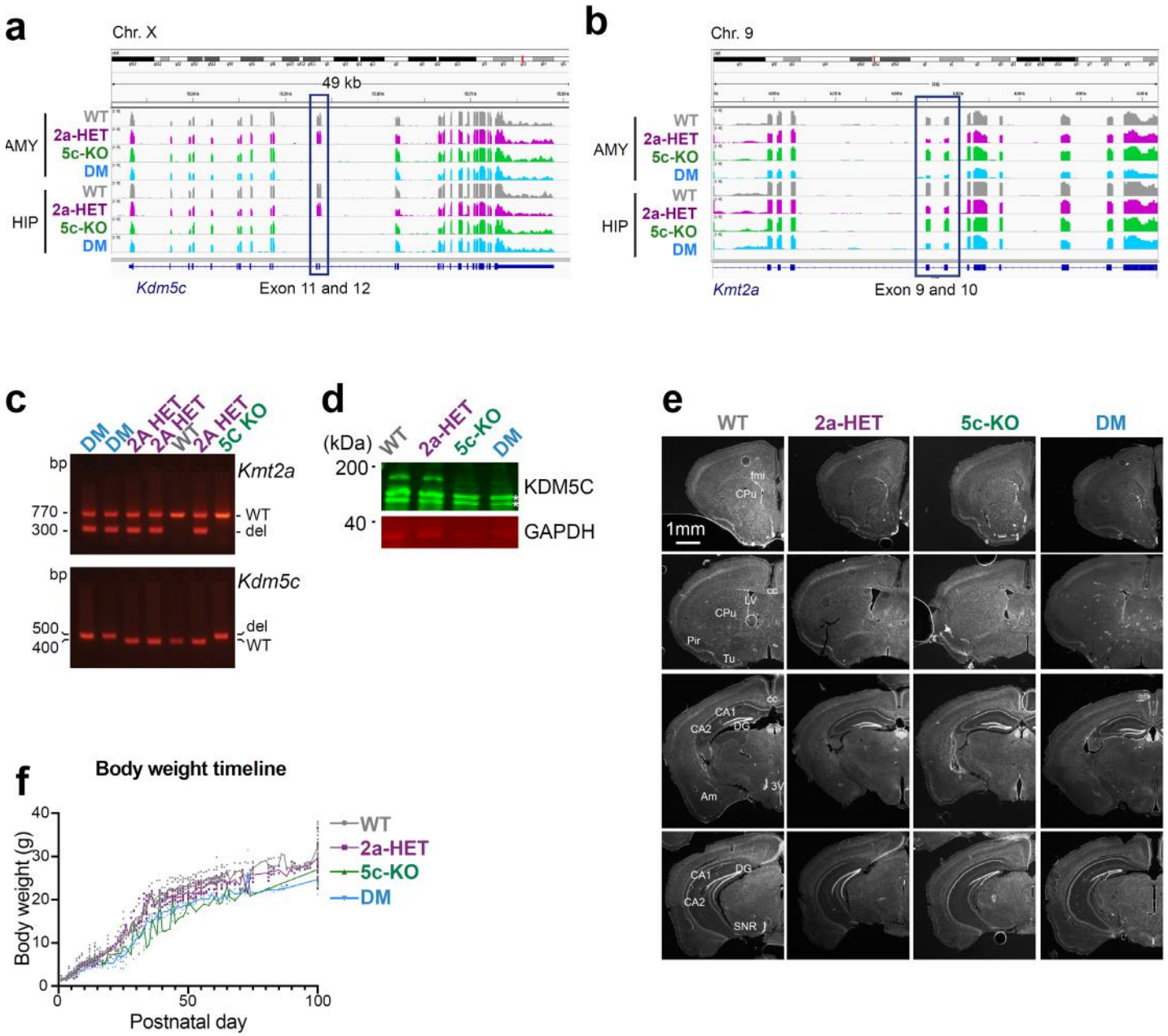

Supplementary Figure 2. Basic features of mutant mice. (A-B) RNA-seq read coverage of *Kmt2a* **(A)** and *Kdm5c* **(B)** genes and targeted exons (highlight) confirmed the intended gene manipulations. **(C)** Genotyping using genomic DNA, confirming presence of *Kmt2a* and/or *Kdm5c* deleted alleles ("del") only in appropriate genotypes. **(D)** Western blot for KDM5C protein. Stars indicate non-specific bands present in all samples. GAPDH shown for equal loading. **(E)** Serial brain sections 30 μm thick stained with DAPI to mark nuclei. Sections shown at Bregma regions 1.41, 0.49, -2.15, and -2.91 mm (top to bottom). Regions highlighted: anterior forceps of the corpus callosum (fmi), caudate putamen (CPu), corpus callosum (cc), lateral ventricle (LV), piriform cortex (Pir), olfactory tubercle (Tu), hippocampal fields CA1 and CA2, dentate gyrus (DG), anteromedial nucleus (AM), third ventricle (3V), substantia nigra pars reticularis (SNR). Scale bar: 1mm. **(F)** Body weight tracked from birth, postnatal day 1 (P1).

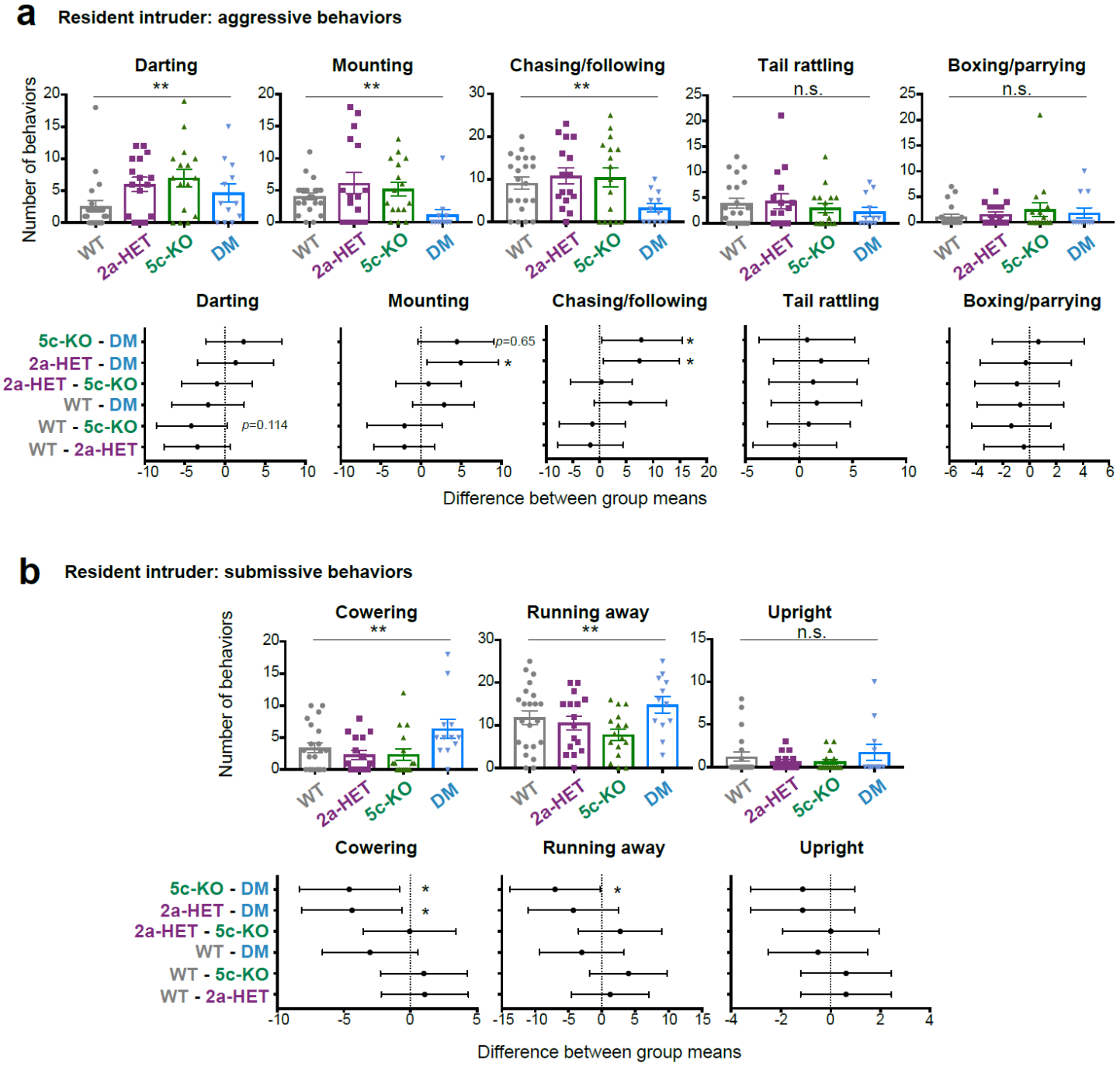

Supplementary Figure 3. Individual behavior types in the resident intruder test. (A) Individual aggressive behaviors (mean ± SEM, $^{**}p < 0.01$ in one-way ANOVA). N.S. depicts no statistical difference. Left panel: average number of all submissive behaviors (mean ± SEM, $^{*}p < 0.05$ in one-way ANOVA). Right panel: Difference between group means of submissive behaviors (mean ± 95% confidence intervals, $^{*}p<0.05$, $^{**}p<0.01$). **(B)** Individual submissive behaviors (mean ± SEM, $^{**}p < 0.01$ in one-way ANOVA). N.S. depicts no statistical difference. N=21 WT, N=16 *Kmt2a*-HET, N=16 *Kdm5c*-KO, and N=12 DM animals were used for all studies. Differences between group means all aggressive **(A)** and submissive **(B)** behaviors (mean ± 95% confidence intervals, $^{*}p<0.05$).

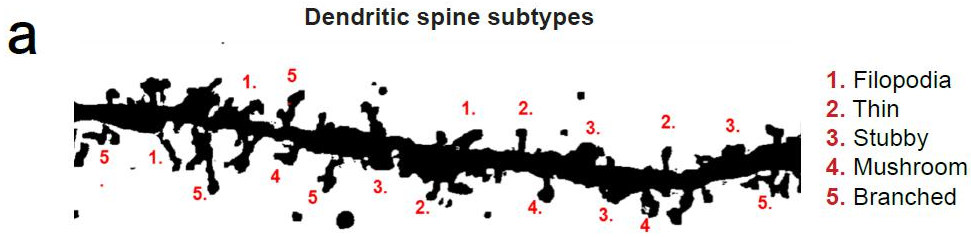

Supplementary Figure 4. Schematic of dendrite spine subtype analysis. (A) Projection image of a dendritic segment from a series of Z stack images derived from BLA pyramidal cells. Numerical marks adjacent to corresponding spine subtypes, represented as: 1. Filopodia, 2. Thin, 3, Stubby, 4. Mushroom, and 5. Branched.

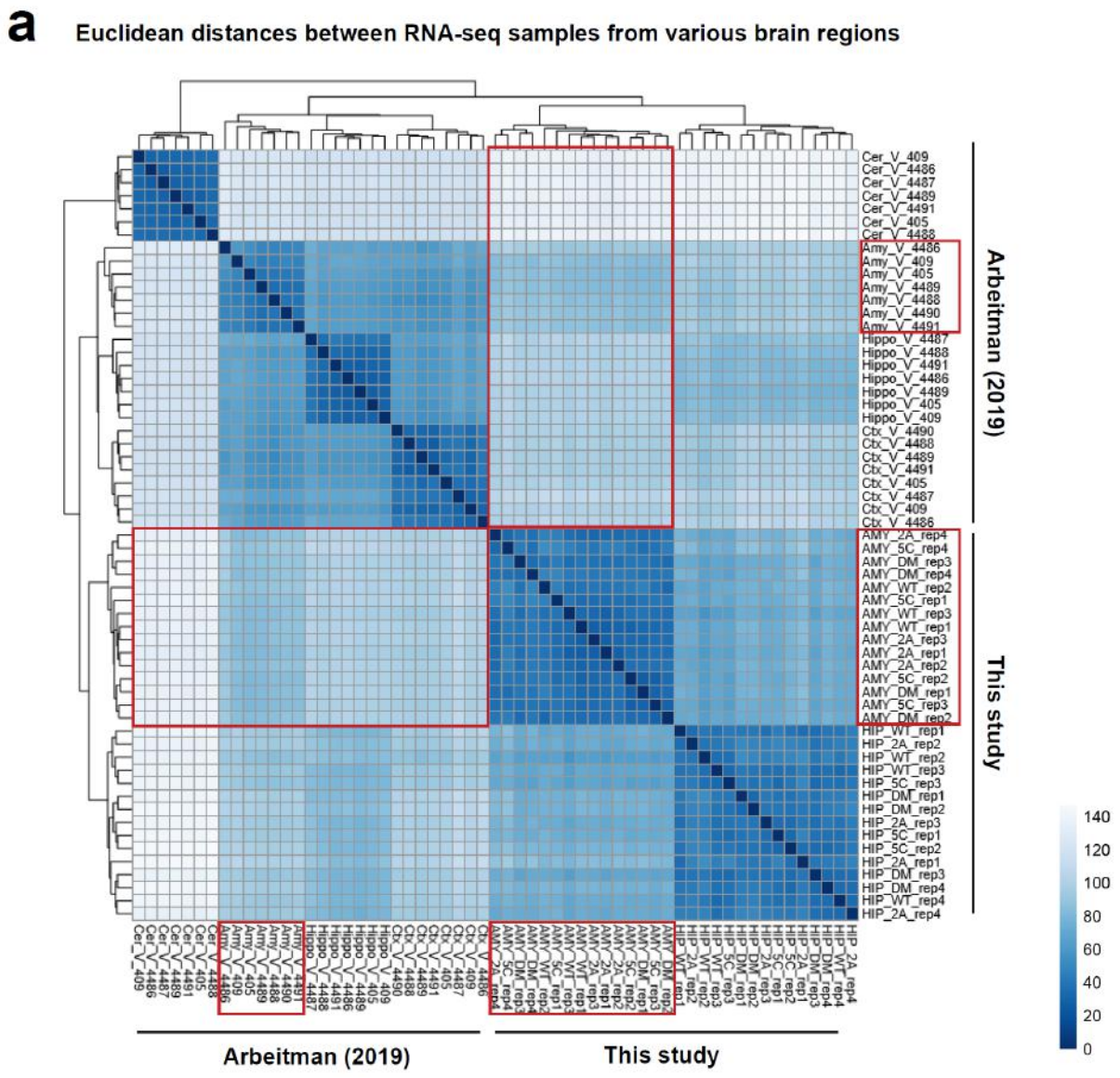

Supplementary Figure 5. Validation of brain microdissection. (A) To validate accuracy of our brain microdissection, we compared our RNAseq data of the hippocampus (HIP) and amygdala (AMY) with those of the Arbeitman paper (5), which involved the hippocampus (Hippo), amygdala (Amy), cerebellum (Cer), cerebral cortex (Ctx). Euclidian distance between all combination of RNA-seq data are plotted (see method). Samples from this study and the Arbeitman study are clustered separately, likely due to difference in experimental procedures and/or sex of mice. Our study used adult male mice, while the Arbeitman study used adult females. Nonetheless, our amygdala samples showed the shortest distance to the Arbeitman amygdala data compared to any other brain tissues (red rectangles). Likewise, our hippocampus data are closest to the Arbeitman hippocampus data among the four brain regions. The data demonstrate that the microdissection of brain regions in the two studies are consistent with each other.

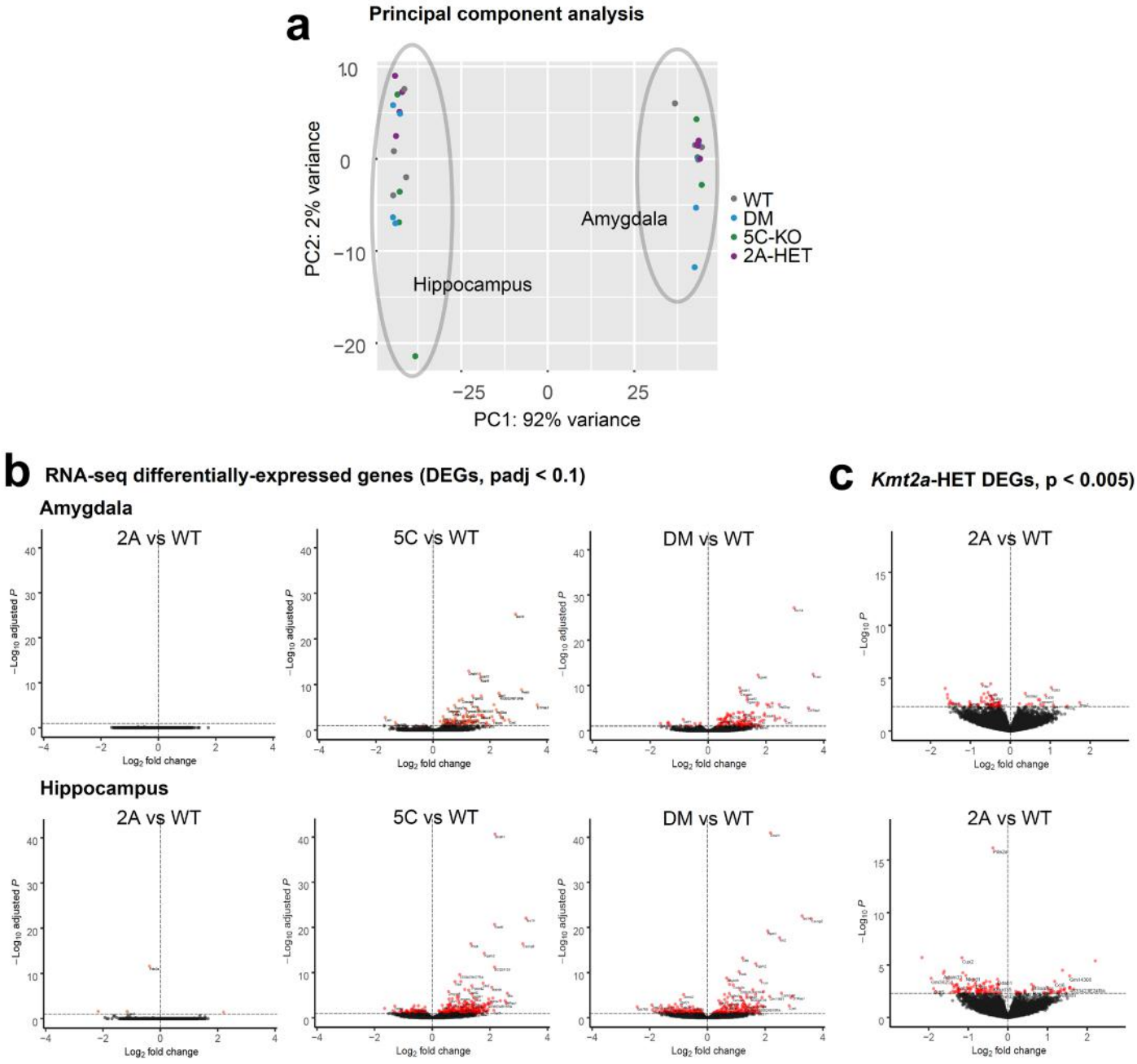

Supplementary Figure 6. Basic analysis of RNA-seq data. (A) PCA analysis of RNA-seq libraries. Tissue types are a stronger segregating factor than genotypes. **(B)** Volcano plot representation of differential expressed genes (DEGs) in mutant vs WT comparisons. Red dots: DEGs with *padj* < 0.1 (see Table S1). **(C)** Mildly dysregulated genes in Kmt2a-HET were recovered with a relaxed threshold.

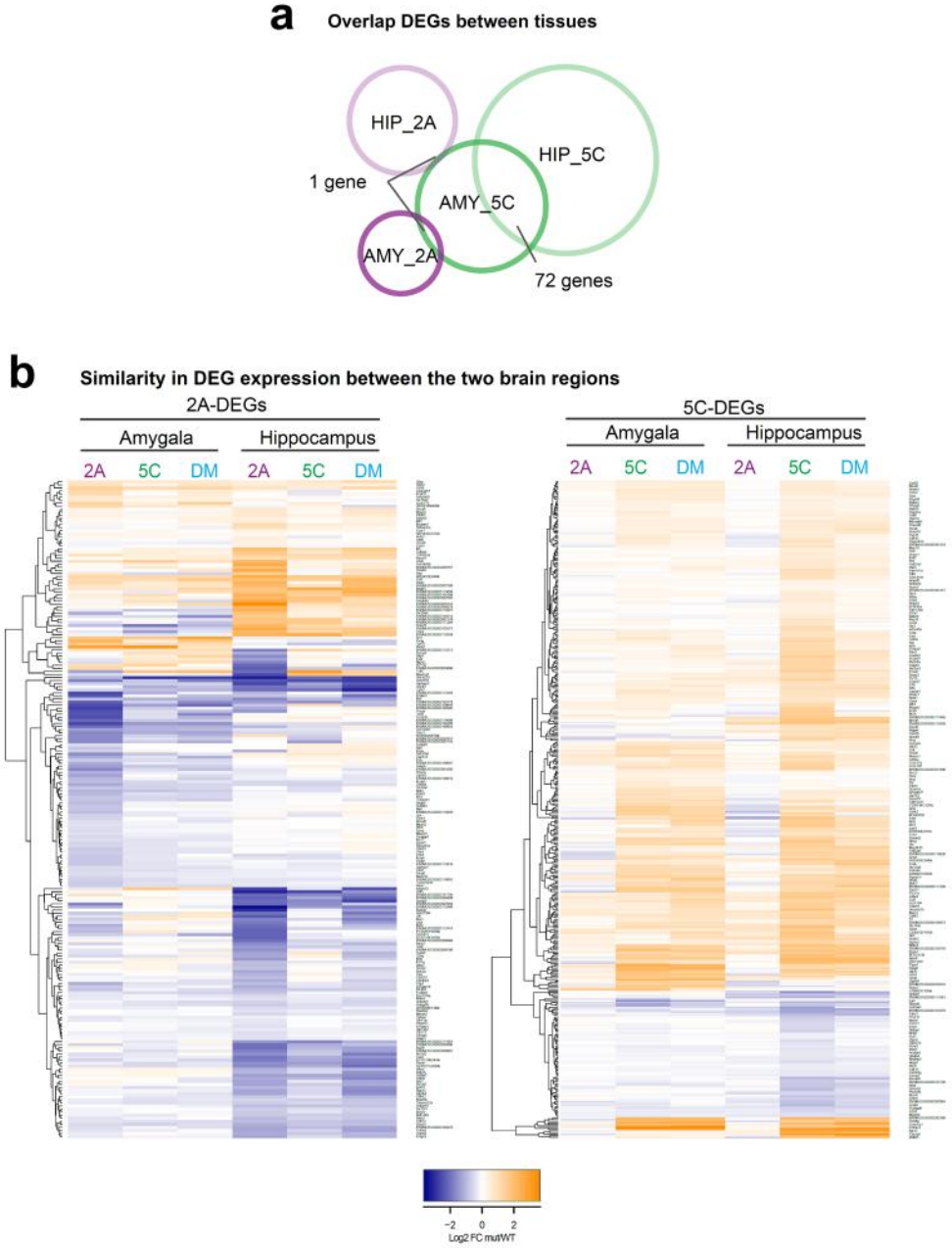

Supplementary Figure 7. Similarity of gene misregulation between the amygdala and hippocampus. (A) Overlap of single mutant DEGs between the amygdala (AMY) and hippocampus (HIP). 5C-DEGs overlap between the two brain regions. **(B)** Heatmap representation of log2 fold changes of 2A-DEGs (left) and 5C-DEGs (right). Overall the patterns of gene misregulation are similar in the two brain regions.

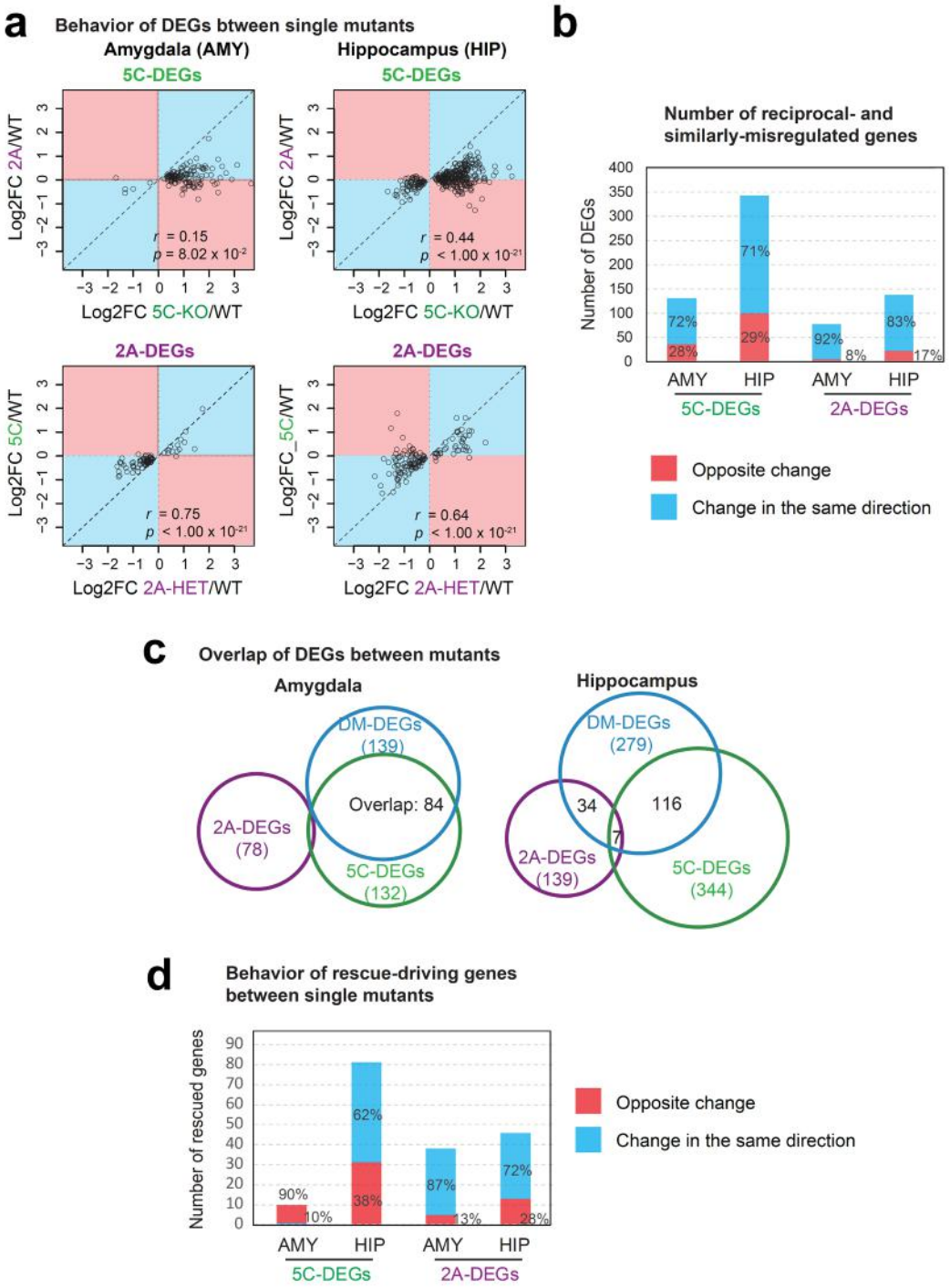

Supplementary Figure 8. Direction of gene misregulation between *Kmt2a*-HET and *Kdm5c*-KO and their overlap in DM brain tissues. (A) Behavior of single-mutant DEGs in the other single mutant. Log2 fold changes of DEGs found in a single mutant were plotted as a function of log2 fold changes in the other single mutant. Red shade covers genes that are regulated in the opposite direction between *Kmt2a*-HET and *Kdm5c*-KO brain tissues. Blue shade covers deregulated genes in the same direction. **(B)** The larger number of genes is dysregulated in the same direction between the two single mutants. **(C)** Overlap of DEGs between mutants. 5C- and DM-DEGs overlap substantially.

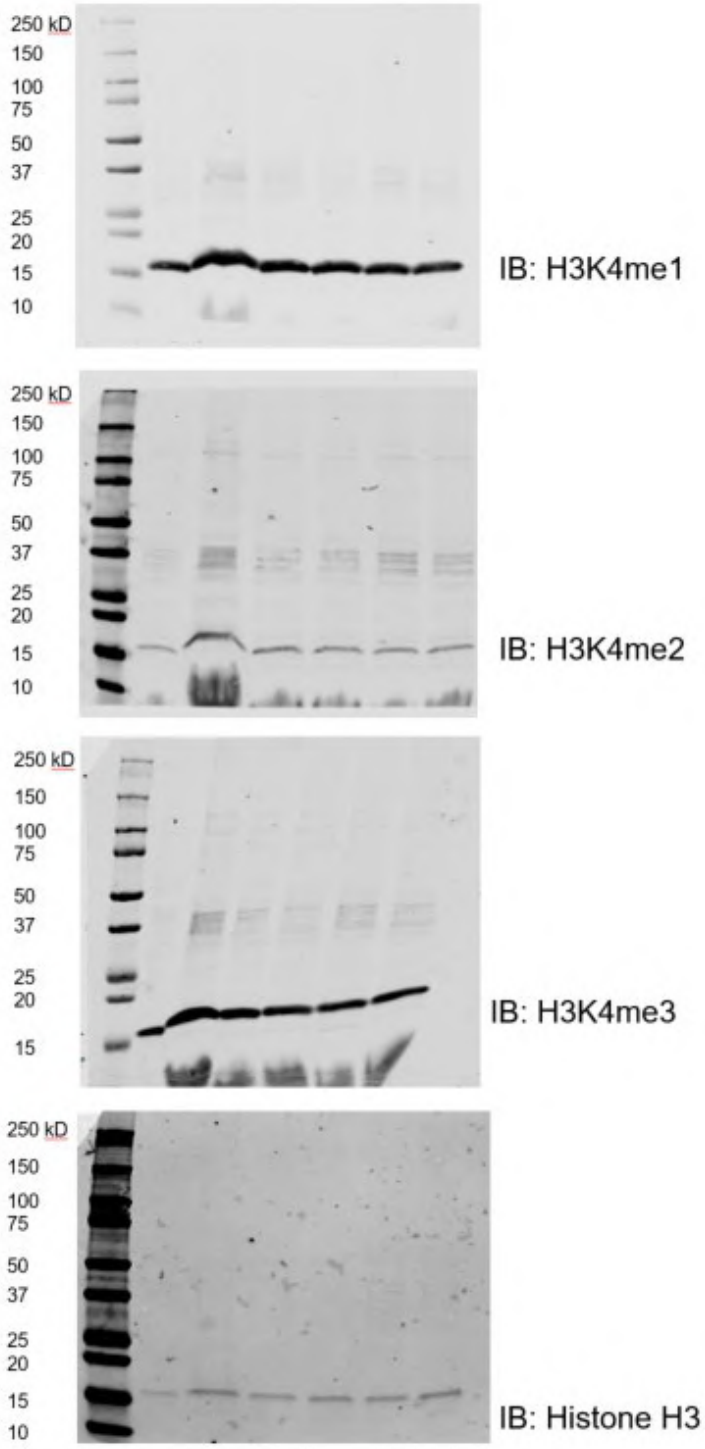

Supplementary Figure 9. Full blots of immunoblot (IB) analyses shown in Figure 6a.

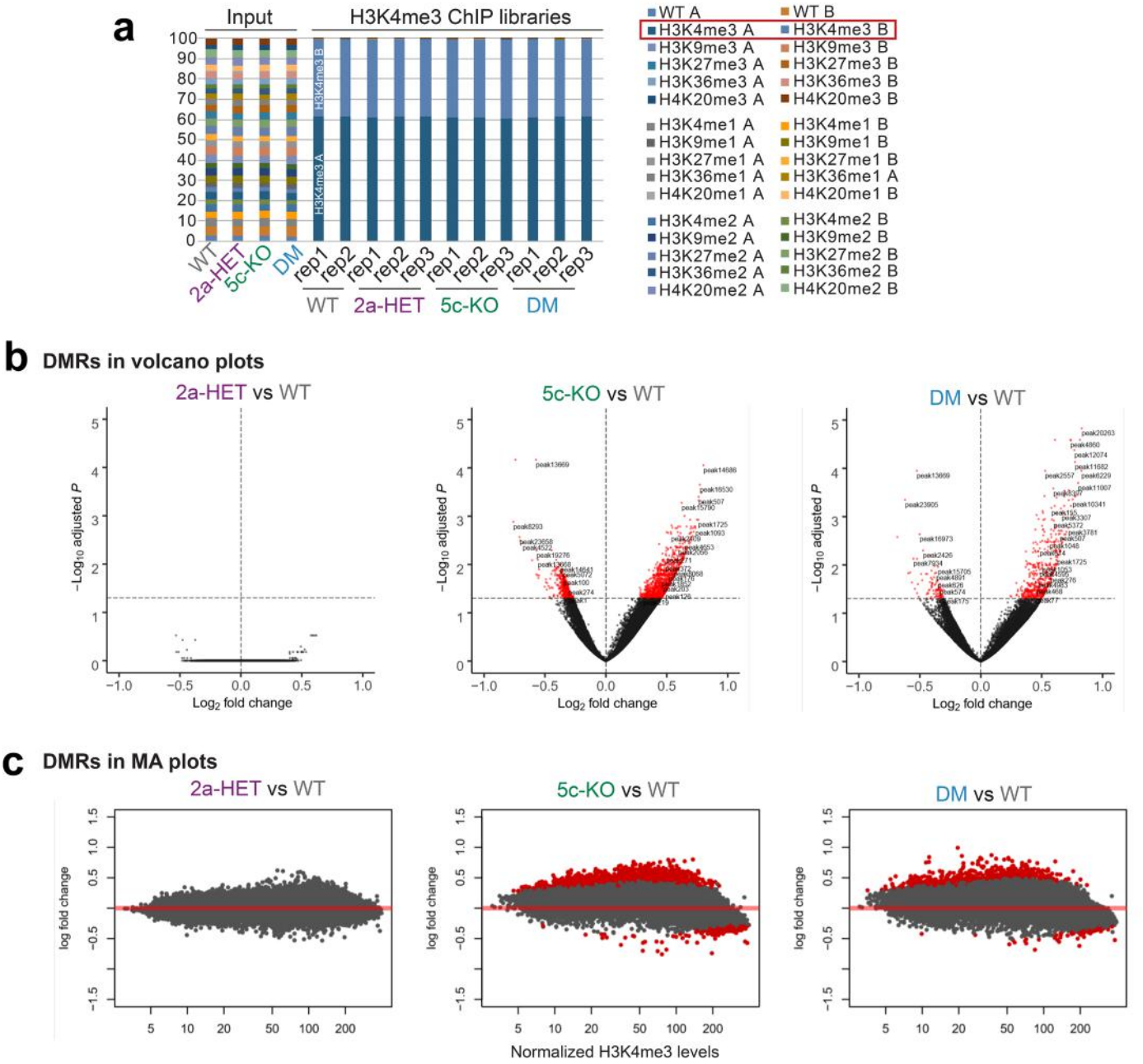

Supplementary Figure 10. Basic characterization of H3K4me3 ChIP-seq data. (A) Validation of H3K4me3 ChIP-seq specificity. Barcode reads originating from spike-in nucleosomes were counted. The two synthetic nucleosomes with the H3K4me3 barcodes dominated all ChIP samples, with H3K4me1/2 nucleosomes rarely detected. **(B)** Volcano plot represents the statistical significance of differentially methylated regions (DMRs). **(C)** MA plots of DMRs revealed signal intensity-dependent misregulation of H3K4me3 in *Kdm5c*-KO, where hypomethylated regions in the mutant were highly methylated in WT.

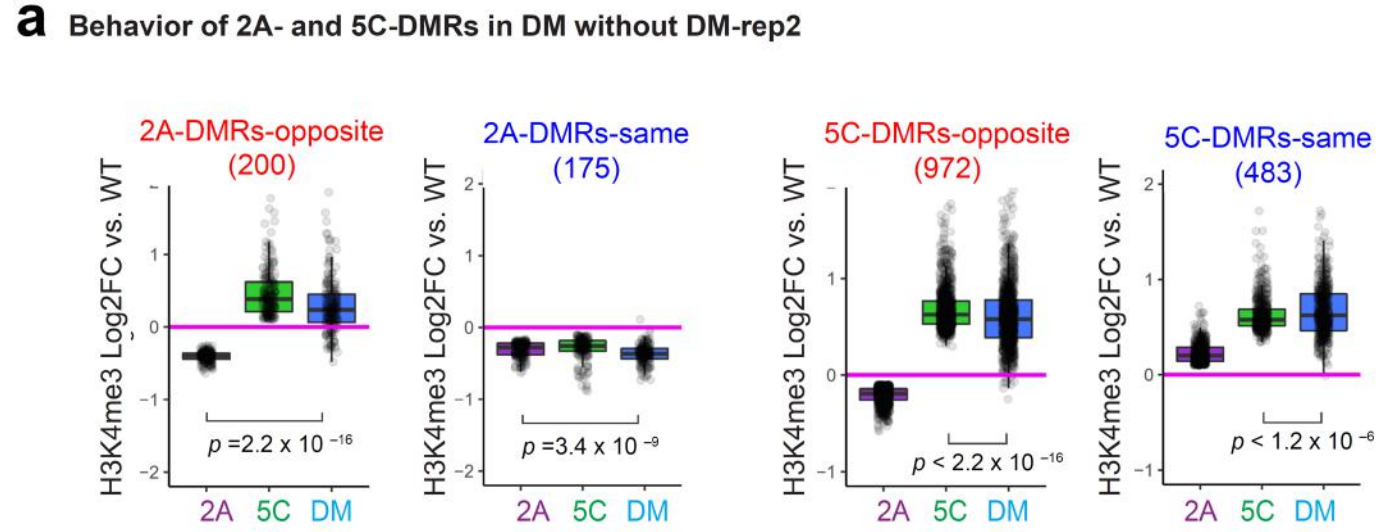

Supplementary Figure 11. Rescue effect without DM rep2. (A) DM rep2 showed strong rescue effect (Figure 6B). To test if H3K4me3 misregulations were alleviated in other DM replicates, we removed DM rep2 and then examined the behavior of single-mutant DMRs in DM. Log2 fold change of DMRs relative to WT were plotted across the three mutants. Boxplot features: box, interquartile range (IQR); bold line, median; gray dots, individual genes. Associated *p* values result from Wilcoxon signed-rank tests. Rescue effects were still evident in DM and also dependent on the direction of misregulation between the single mutants.

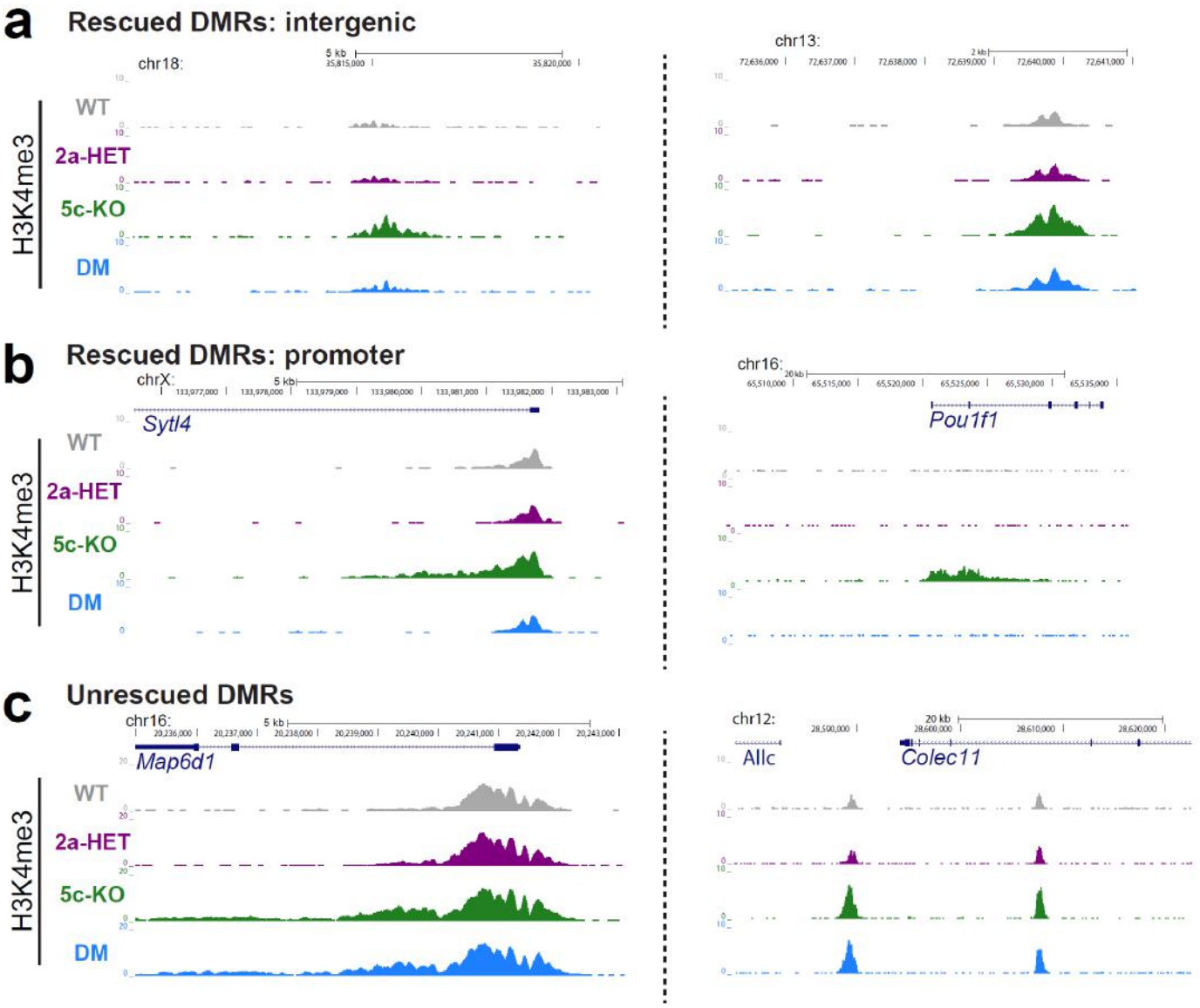

Supplementary Figure 12. Representative loci found in the H3K4me3 ChIP-seq analysis. (A) Representative genome browser view of two representative loci for each of the major genome areas: rescued intergenic DMRs **(A)**, rescued promoter DMRs **(B)**, un-rescued DMRs **(C)**. Represented H3K4me3 patterns are averaged signals of replicates that are normalized to read depth and spike-in nucleosome signals.

References

1. Tasic B, Menon V, Nguyen TN, Kim TK, Jarsky T, Yao Z, et al. Adult mouse cortical cell taxonomy revealed by single cell transcriptomics. *Nat Neurosci.* 2016;19(2):335-46.

2. Lein ES, Hawrylycz MJ, Ao N, Ayres M, Bensinger A, Bernard A, et al. Genome-wide atlas of gene expression in the adult mouse brain. *Nature.* 2007;445(7124):168-76.

3. Kang HJ, Kawasawa YI, Cheng F, Zhu Y, Xu X, Li M, et al. Spatio-temporal transcriptome of the human brain. *Nature.* 2011;478(7370):483-9.

4. Pletikos M, Sousa AM, Sedmak G, Meyer KA, Zhu Y, Cheng F, et al. Temporal specification and bilaterality of human neocortical topographic gene expression. *Neuron.* 2014;81(2):321-32.

5. Arbeitman MN. Maternal Experience Leads to Lasting Gene Expression Changes in Some Regions of the Mouse Brain. *G3 (Bethesda).* 2019;9(8):2623-8.